A Numerical Investigation of Several Factors Contributing to the Observed Variable Intensity of Deep Convection over South Florida

GREGORY J. TRIPOLI AND WILLIAM R. COTTON

Department of Atmospheric Science, Colorado State University, Fort Collins 80523

ABSTRACT

This study employs a revised version of the Colorado State University three-dimensional numerical cloud scale model to investigate the observed behavior of deep convection over South Florida on 17 July 1973. A brief description of recent model improvements is made. A combined balance and dynamics initialization procedure designed to introduce variable magnitudes and distributions of low-level wind convergence to the initial fields is described.

Using radiosonde and PIBAL data collected by the NOAA/ERL Florida Area Cumulus Experiment (FACE) and the National Weather Service at Miami on 17 July 1973, composite wind, temperature, pressure and moisture profiles were constructed to depict the state of the atmosphere at the time of deep convection. Mesoscale convergence was estimated from results of a mesoscale model simulation of low-level sea breeze convergence made by Pielke (personal communication) for the same case study day. Several numerical simulations were performed using the sounding data as a basic state. The initial magnitude and distribution of low-level convergence was varied and the sensitivity of the model to some microphysical parameters was examined.

The results of the numerical experiments show that (i) the magnitude of surface convergence over a finite area has a pronounced influence on the simulated storm circulation, the eddy kinetic energy of the storm and the total rainfall of the storm system; (ii) the horizontal distribution of convergence has a relatively large effect on the rates of entrainment into the updraft below 5 km MSL resulting in significant modulations in predicted precipitation, but only moderate changes in storm kinetic energy; (iii) variations in terminal velocity of precipitation associated with the introduction of the ice phase has only a minor effect on precipitation and total kinetic energy of the storm; and (iv) increased rain evaporation rates result in a moderate increase in the kinetic energy of the simulated storm, but at the expense of surface precipitation. Pressure forces are also shown to play an important role in initiating downdrafts and in biasing the direction of downdraft-associated outflow. Implications of these results to the modification of convective clouds are discussed.

1. Introduction

The results of The Thunderstorm Project reported by Byers and Braham (1948) first described how cumulus cloud formations over Florida were seemingly closely tied to the diurnal sea breeze circulation. Later, numerical mesoscale model simulations of the diurnal sea breeze circulation over South Florida performed by Pielke (1974) were shown to produce patterns of low-level convergence consistent with satellite- and radar-observed cloud and precipitation patterns. In a subsequent study by Cotton et al. (1976), important modifications to the environment produced by Pielke's simulations were documented and discussed in relation to their effect on convection. These modifications included perturbation of the thermodynamic profile, increase in depth of the planetary boundary layer, change in the vertical shear of the horizontal wind, and development of intense regions of horizontal convergence of heat, moisture and momentum. One-dimensional

cloud model simulations indicated that the altered thermodynamic profiles produced substantially deeper and more intense convection than the unaltered profiles. In a more recent study, Ulanski and Garstang (1978a) presented convincing observational evidence that surface convergence patterns nearly always precede the development of radar echos for periods as long as 90 min over southern Florida. In that work, they suggested that "the most crucial factors in determining the total amount of rainfall produced by a given storm is the size of the area of surface convergence." They also concluded that, while the smaller storms of 5–10 km² appeared to be almost totally at the mercy of the initial convergence, larger storms of 50 km² exhibited some ability to alter their own environment by enhancing surface convergence. It was pointed out that the larger storms appeared to be much more efficient than smaller storms in converting low-level moisture convergence to precipitation.

The response of cumulus to mesoscale induced

convergence was also investigated by Chang and Orville (1973) and Chen and Orville (1979), who employed two-dimensional cloud simulations. These papers have demonstrated enhanced convection in the presence of some imposed mean vertical motion.

In this paper, we examine several factors which may have contributed to the variable behavior of cumulus clouds observed over south Florida on 17 July 1973. A series of three-dimensional numerical experiments are performed in which the sensitivity of the predicted cloud organization and intensity to variations in mesoscale convergence and alterations in cloud microphysical parameters is tested.

2. Description of the three-dimensional cumulus model

In order to study the complex dynamic interaction between cumulus-scale motions and the large-scale thermodynamic and dynamic fields, a three-dimensional cumulus convection model was developed. An earlier version of this model was discussed by Cotton and Tripoli (1978). Since then the model has undergone a number of improvements. The present formulation and finite-differencing techniques are discussed in this section. The present model utilizes a vertical coordinate transformation described by Gal-Chen and Somerville (1975a,b) and Clark (1977). Since the coordinate transformation is not exercised in the relatively flat terrain over south Florida, we will not describe it herein. Moreover, because the simulations are performed on the time scale of 1 h, the Coriolis force is also neglected.

In formulating a predictive set of primitive equations, eight time-dependent variables are considered. Each variable is averaged with respect to a resolvable scale and compared to a given horizontally homogeneous reference state as described by Cotton and Tripoli (1978). The predictive variables are the Cartesian velocity components $\bar{u}$, $\bar{v}$, and $\bar{w}$, the pressure deviation from its reference state $\bar{p}'$, the potential temperature $\bar{\theta}$, and the mixing ratios of water vapor ($\bar{q}_v$), cloud water ($\bar{q}_c$) and rainwater ($\bar{q}_r$). The rainwater mixing ratio has been added since the study of Cotton and Tripoli (1978) for use in precipitating cloud studies. At present, there is no provision for modeling the ice phase, although testing of such a parameterization is now complete and will be considered in later studies.

a. The governing equations

The prognostic momentum equations are given by

$$\frac{\partial \bar{u}_i}{\partial t} + \alpha_0 \frac{\partial p'}{\partial x_i}$$

$$= \text{ADV}(\bar{u}_i) + \text{TURB}(\bar{u}_i) - \delta_{i3} g \frac{\bar{p}'}{\rho_0} = \text{RU}_i, \quad (1)$$

where the advective operator (ADV) and turbulence operator are defined later in this section (See Appendix for list of symbols.). The density $\bar{\rho}'$ is diagnosed from the equation of state by

$$\rho' = \rho - \rho_0 = \frac{(\bar{p}' + p_0)^{1/\gamma}}{R\bar{\theta}p_r^\kappa(1 + 0.61\bar{q}_v)} - \rho_0. \quad (2)$$

The symbol RU$_i$ represents the right-hand side of the equation which is integrated on the longer time step as described by Cotton and Tripoli (1978) and reiterated later in this paper. Poisson's equation given by

$$\frac{T}{\theta} = \left(\frac{p}{p_r}\right)^\kappa \quad (3)$$

has been assumed.

The perturbation pressure tendency equation is given by

$$\frac{\partial \bar{p}'}{\partial t} + \gamma p_0 \frac{\partial u_i}{\partial x_i} = \text{ADV}(\bar{p}' + p_0) + \text{TURB}(\bar{p}')$$

$$+ \frac{\gamma p_0}{\theta_{v0}} \left[0.61\bar{\theta} - \frac{L_{vl}}{C_p T}(1 + 0.61\bar{q}_v) \right]$$

$$\times \left[\delta_m \frac{d\bar{q}_s}{dt} + E \right] = \text{RP}, \quad (4)$$

where p_0, ρ_0 and θ_{v0} are the reference state pressure, density and virtual potential temperature. The reference state is hydrostatic and obeys the moist equation of state

$$p_0^{1/\gamma} = \rho_0 R p_r^\kappa \theta_{v0}, \quad (5)$$

where the reference pressure (p_r) is defined at 1000 mb. The delta function δ_m is given by

$$\delta_m = \begin{cases} 1, & \text{saturated} \\ 0, & \text{unsaturated.} \end{cases} \quad (6)$$

The term dq_s/dt is the rate at which vapor is being converted to liquid during moist adiabatic ascent or descent and E is the rate vapor is being produced by evaporation of rain. A description of these processes will be presented later in this section.

The potential temperature tendency is obtained from the irreversible form of the first law of thermodynamics and is given by

$$\frac{\partial \bar{\theta}}{\partial t} = \text{ADV}(\bar{\theta}) + \text{TURB}(\bar{\theta})$$

$$- \frac{L_{vl}}{C_p T}\left(\delta_m \frac{d\bar{q}_s}{dt} - E \right) + \text{SA}_\theta, \quad (7)$$

where SA$_\theta$ is the isobaric saturation adjustment on potential temperature to be described later in this section.

The moisture continuity equations are given by

$$\frac{\partial \bar{q}_v}{\partial t} = \text{ADV}(\bar{q}_v) + \text{TURB}(\bar{q}_v) + \delta_m \frac{d\bar{q}_s}{dt}$$
$$- E + \text{SA}_{\bar{q}_v}, \qquad (8)$$

$$\frac{\partial \bar{q}_c}{\partial t} = \text{ADV}(\bar{q}_c) + \text{TURB}(\bar{q}_c) - \delta_m \frac{d\bar{q}_s}{dt}$$
$$- \text{AUTO} - \text{ACCR} + \text{SA}_{\bar{q}_c}, \qquad (9)$$

$$\frac{\partial \bar{q}_r}{\partial t} = \text{ADV}(\bar{q}_r) + \text{TURB}(\bar{q}_r) - \frac{1}{\rho_0} \frac{\partial(v_T \rho_0 \bar{q}_r)}{\partial z}$$
$$+ E + \text{AUTO} + \text{ACCR} + \text{SA}_{\bar{q}_r}. \qquad (10)$$

The terms AUTO and ACCR represent the auto-conversion and accretion of cloud water to rain-water, the terminal velocity of rain is given by v_T, and the rate of evaporation of rainwater is given by E. A description of the rain parameterization is given in the next section.

The advective operator used in the present model is given by

$$\text{ADV}(\bar{A}) = - \frac{1}{\rho_0} \left[\frac{\partial \rho_0 \bar{u}_i \bar{A}}{\partial x_j} - \bar{A} \frac{\partial}{\partial x_j} (\rho_0 \bar{u}_i) \right]. \qquad (11)$$

This is a more conservative form of the advective operator than that used by Cotton and Tripoli (1978) since the second term on the RHS of (11), or residual term, contains the divergence of momentum which tends toward zero. In a perfectly anelastic deep convection system, the residual term would be identically zero. In the earlier version of the model reported by Cotton and Tripoli (1978), the residual term contained only velocity divergence which, for a deep convective system, would not necessarily be small in magnitude.

The turbulence operator is given by

$$\text{TURB}(\bar{A}) = - \frac{\overline{\partial u_i'' A''}}{\partial x_j}. \qquad (12)$$

The turbulence is assumed to be nondivergent and is parameterized using eddy viscosity theory described by Cotton and Tripoli (1978). The turbulent fluxes of heat, momentum and moisture are described at the lower boundary using the surface layer parameterization described by Manton and Cotton (1977).

b. Moist physics

Latent heating occurs if an air parcel is rising and is saturated with respect to water. The rate of latent heating in (7) is diagnosed assuming moist adiabatic ascent where the rate of change of saturation mixing ratio is given by

$$\frac{d\bar{q}_s}{dt} = \frac{\dfrac{\bar{w}\bar{\theta}\bar{q}_s}{\bar{T}_v} \dfrac{g}{R}\left(\dfrac{\epsilon L_{vl}}{C_p \bar{T}} - 1\right)}{\dfrac{\epsilon L_{vl}^2 \bar{q}_s}{R C_p \bar{T}^2} + 1}. \qquad (13)$$

Because the above formulation does not guarantee that the system will remain very close to saturation in the presence of cloud water and because numerical truncation error may produce negative quantities of mixing ratio, an isobaric saturation adjustment is performed after each time step during integration. The form of adjustment to cloud water is given by

$$\text{ADJ} = \frac{\bar{q}_v - \bar{q}_s}{1 + \dfrac{\bar{q}_s}{T}\left(\dfrac{\epsilon L_{vl}}{R}\right)}. \qquad (14)$$

Keeping this in mind as a minimum upward adjustment to cloud water, the adjustment procedure given below also eliminates negative mixing ratios and eliminates amounts of rainwater mixing ratios less than 1×10^{-6}. The procedure is given by

$$(\text{SA})_{\bar{q}_c} = \text{MAX}(-\bar{q}_c, \text{ADJ}), \qquad (15)$$

$$(\text{SA})_{\bar{q}_r} = \text{MAX}\{-\bar{q}_r, \text{MIN}[\text{ADJ} - (\text{SA})_{\bar{q}_c}, 0]\}, \qquad (16)$$

$$(\text{SA})_{\bar{q}_v} = \text{MAX}[-\bar{q}_v, -(\text{SA})\bar{q}_c - (\text{SA})_{\bar{q}_r}], \qquad (17)$$

$$(\text{SA})_{\bar{\theta}} = - \frac{\bar{\theta} L_{vl}}{C_p \bar{T}} (\text{SA})_{\bar{q}_r}. \qquad (18)$$

This adjustment will allow no mixing ratios to fall below zero, while conserving water at a grid point. If, before adjustment, the predicted total net water at a grid point is less than zero, water conservation is sacrificed in the interest of guaranteeing positive definite water. This has been found to occur at times in the upper troposphere where falling rainwater leaves negative amounts of rain mixing ratios due to truncation error of centered spatial differencing schemes which cannot be compensated by existing low vapor mixing ratios. These adjustments are found to be small, however.

c. The precipitation parameterization

As mentioned earlier, the model contains only a warm-cloud precipitation process at this stage of development. The precipitation parameterization basically follows the general philosophy outlined by Kessler (1969) in which total liquid water is divided into two parts: cloud water, which is assumed to move with the air, and rain, which is allowed to translate relative to the air. Rainwater is envisaged to increase by two processes: auto-conversion, which is largely a parameterization of the effects of the cloud droplet collection process, and the accretion of cloud droplets by raindrops.

Similar to Kessler, we assume that the spectral density of rain is given by the Marshall-Palmer spectrum. The parameterizations differ somewhat from Kessler as a consequence of reexamining the physical basis of the approximations. A detailed development of the parameterizations can be found in Manton and Cotton[1] (hereafter referred to MC).

The conversion term (AUTO) accounts for the initial generation of rain by the coalescence between cloud droplet pairs to form raindrops. This process is expressed in the form

$$ \text{AUTO} = f_c q_c h(\bar{q}_c - q_{cm}), \qquad (19) $$

where f_c represents the mean collision frequency for cloud droplets which become raindrops after colliding, $h(x)$ is the Heaviside unit stepfunction and q_{cm} is the minimum cloud-water mixing ratio below which there is no conversion. It is assumed that droplets become large enough for significant coalescence to begin when the mean droplet radius is equal to r_{cm}. This gives

$$ q_{cm} = {}^4\!/_3 \pi \rho_w r_{cm}{}^3 N_c/\rho_0, \qquad (20) $$

where ρ_w is the density of water and N_c is the mean cloud droplet concentration. In this study, we have taken N_c to be 3×10^8 m^{-3}. For the purposes of these calculations, a value of $r_{cm} = 10^{-5}$ m is assumed. Once $\bar{q}_c$ exceeds q_{cm}, MC estimated the mean collision frequency as

$$ f_c = \pi r_c{}^2 E_c V_c N_c. \qquad (21) $$

The parameter r_c is the cloud droplet radius corresponding to the mean droplet mass ($\bar{x} = \bar{q}_c \rho_0/N_c$), E_c is the mean collection efficiency for droplets involved in the conversion process (where it is assumed $E_c = 0.55$), and V_c is the mean terminal velocity of the cloud droplets estimated from Stokes law. The resultant mean autoconversion rate is given by

$$ \text{AUTO} = \frac{0.104 g E_{cR} \rho_0{}^{4/3}}{\mu (N_c \rho_w)^{1/3}} \bar{q}_c{}^{7/3} h(\bar{q}_c - q_{cm}). \qquad (22) $$

The present parameterization produces an initially more gradual conversion rate than does Kessler's, but at high cloud water mixing ratios it produces a much more rapid conversion. The main advantage of this parameterization is that it does not significantly sacrifice the simplicity of the parameterization as sought by Kessler while allowing the capability of responding to differing air masses. It does not, however, allow a time delay in the conversion process as sought by Cotton (1972). As a result,

the simulation of observed weak echo regions in rapidly rising updrafts may not be possible.

The process of raindrop accretion of cloud droplets and raindrop motion through the air is parameterized by assuming that the raindrop spectral density $\phi(r)$ is exponentially distributed (Marshall and Palmer, 1948) in the form

$$ \phi(r) = (N_R/R_m) \exp(-r/R_m), \qquad (23) $$

where N_R represents the raindrop concentration and R_m is a characteristic radius for the distribution. In contrast to Kessler, it is assumed that the slope of the distribution $(1/R_m)$ is a constant, whereas the intercept parameter

$$ N_0 = N_R/R_m \qquad (24) $$

varies. MC justified this assumption on the basis of the experiments by Blanchard and Spencer (1970) which suggest that the Marshall-Palmer distribution is an asymptotic spectral density produced by a balance between coalescence, tending to increase the size of an individual drop and drop breakup, tending to reduce the drop size. More recently, Srivastava (1978) showed by numerical experiment that the slope of (23) tends toward constant values when collisional breakup becomes dominant. He showed that this occurred when the rainwater mass density exceeded 10^{-3} kg m^{-3}.

By integrating the mass spectral density $x(r)\phi(r)$, where $x(r)$ represents the mass of a droplet of radius r, over the entire distribution, one can show that

$$ N_R = \frac{\bar{q}_r \rho_0}{8\pi \rho_w R_m{}^3}. \qquad (25) $$

Thus, consistent with the findings of Srivastava (1978), N_R/R_M is proportional to the rainwater content. Using the data of Hudson (1963), Mueller and Sims[2] and Blanchard and Spencer (1970), MC estimated R_m is $\sim 2.7 \times 10^{-4}$ m. This value of R_m is used in the numerical experiments described below. The terminal velocity of raindrops is given by

$$ V(r) = \alpha(\rho_w/\rho_0)^{1/2}(gr)^{1/2}, \qquad (26) $$

where α is estimated to be 2.13 based on the data of Gunn and Kinzer (1949).

The movement of $\bar{q}_r$ relative to the air is then given by

$$ F_R = \int_0^\infty \rho_0 {}^4\!/_3 \pi r^3 \rho_w V(r) \phi(r) dr, \qquad (27) $$

which on substituting (26), (25) and (23), and in-

[1] Manton, M. J., and W. R. Cotton, 1977: Formulation of approximate equations for modeling moist deep convection on the mesoscale. Atmos. Sci. Pap. No. 266, Colorado State University, NSF Grant DES 7513310, 62 pp.

[2] Mueller, E. A., and A. L. Sims, 1966: Relationships between reflectivity, attenuation and rainfall rates derived from drop size spectra. Tech. Rep. ECOM-00032-F, Illinois State Water Survey, Contract DA-28-043, AMC-00032(e), 112 pp.

tegrating, gives us

$$F_R = v_T q_r, \qquad (28)$$

where

$$v_T = \frac{1}{6}\Gamma(4.5)V(R_m) = 1.94V(R_m).$$

Thus under the assumption of a constant slope for (23), the effective terminal velocity of the rain is independent of the rain density. When $R_m = 2.7 \times 10^{-4}$ m and $\rho_0 = 1.28$ kg m^{-3}, this velocity is 5.93 m s^{-1}. This should be compared with Kessler's effective velocity estimate which varies slowly with rainwater content ranging from 5.13 to 7.49 m s^{-1} as the rainwater mass density increases from 1×10^{-3} to 20×10^{-3} kg m^{-3}.

By integrating the rate of increase in mass of a single drop of radius r due to accretion over the entire distribution (23), similar to Kessler, MC found

$$\text{ACCR} = 0.884 E_{cr}\left(\frac{g\rho_0}{\rho_w R_m}\right)^{1/2} \bar{q}_c \bar{q}_r. \qquad (29)$$

This differs from Kessler who found the accretion was proportional to $q_r^{0.875}$. With $E_{cR} = 1.0$, the present result gives lower accretion rates than does Kessler's when the water mass density is less than 2.28×10^{-3} kg m^{-3}; however, the differences are not large at moderate rain densities. Although MC assumed that E_{cR} was unity, its application to this model resulted in the complete elimination of $\bar{q}_c$ near the lateral boundaries of the cloud. This cosmetically annoying feature was removed by estimating E_{cR} by adopting the potential flow solutions of Langmuir (1948) in the form

$$E_{cR} = \begin{cases} 0 & \text{for} \quad \text{STK} < 0.0833, \\[2mm] \dfrac{\text{STK}^2}{(\text{STK} + \frac{1}{2})^2} & \text{for} \quad \text{STK} \geq 0.0833. \end{cases} \qquad (30)$$

The parameter STK is the Stokes number which is estimated from the characteristic raindrop radius R_m and cloud droplet radius r_c giving

$$\text{STK} = \frac{0.22\rho_w V(R_m)\bar{q}_c^{2/3}}{R_m\mu}\left[\frac{0.239}{N_c/3}\right]^{2/3}. \qquad (31)$$

In order to be consistent with the data of Weickmann and Aufm Kampe (1953), the cloud droplet concentration N_c in the denominator of the term in square brackets of (31) is reduced by two-thirds to account for depletion of cloud droplets by raindrop accretion once substantial $\bar{q}_r$ forms. It should be noted that more accurate estimates of E_{cR} can be obtained by using the interpolation scheme developed by Beard and Grover (1974). We would have to determine if the model is sufficiently sensitive to E_{cR} to justify the added computational expense of their scheme, however.

Finally, the rate of change of $\bar{q}_r$ due to evapora-

tion of raindrops (E) is derived by integrating over the raindrop distribution (23) the rate of evaporation of a single raindrop (see Byers, 1965), i.e.,

$$\frac{dx(r)}{dt} = 4\pi r G(T,P)(S - 1)(1 + F \text{ Re}^{1/2}), \qquad (32)$$

where $(S - 1)$ is the supersaturation, F the ventilation coefficient taken to be 0.21, and Re the Reynold's number. The function $G(T,P)$ is defined as in Byers (1965) as

$$G(T,P) = \frac{1}{\dfrac{m_w L_{vl}^2}{kR_* T^2} + \dfrac{R_* T}{e_s(T)Dm_w}},$$

where m_w is the molecular weight of water, k the molecular diffusivity of heat, R_* the universal gas constant, D the molecular diffusivity for water vapor and $e_s(T)$ the saturation vapor pressure over a plain pure water surface at T. Defining

$$\text{Re} = \frac{2rV(r)\rho_0}{\mu}, \qquad (33)$$

where $V(r)$ is obtained from (26), and substitution of (32), (33) and (33) into

$$E = \frac{1}{\rho_0}\int_0^\infty \frac{dx(r)}{dt}\, \phi(r)dr \qquad (34)$$

gives us, after integration,

$$E = \left\{0.5 + 0.349\left[\frac{(\rho_w g \rho_0 R_m^3)^{1/4}}{\mu^{1/2}}\right]\right\}$$
$$\times \frac{G(T,P)}{R_m^2\rho_w}(S - 1)\bar{q}_r. \qquad (35)$$

This should be compared to Kessler's evaporation rate equation which is proportional to $\bar{q}_r^{0.65}$. Because the present result explicitly accounts for the Reynolds number dependence of the evaporation rate from a falling drop, it produces higher values of E when the rainwater density is $\geq 6 \times 10^3$ kg m^{-3}.

d. Grid system and finite differencing

A staggered grid system discussed by Cotton and Tripoli (1978) was used where the number of grid points in the x, y, z directions and their spacing can be arbitrarily defined. For this case study, 48 grid points were used in the x and y direction and 24 in the z direction. The spacing was set at a constant 750 m in all directions for a total domain size of 35.25 km $\times$ 35.25 km in the horizontal, and 17.25 km in the vertical.

The effects of numerical truncation error are minimized by applying the fourth-order space differencing described by Grammeltvedt (1969) to the

advection of all quantities and flux divergence of rain due to terminal velocity. At points adjacent to boundary points, second-order differencing was used because a lack of enough information to compute the fourth-order derivative. The finite-difference technique applied to boundary points is described below. All other derivatives which include the pressure gradient, flux divergence of subgrid-scale turbulence, deformation calculations and divergence calculations were made using second-order centered space differencing.

The same time-split, leapfrog time-differencing scheme described previously (Cotton and Tripoli, 1978) is used in this study. In this scheme the higher frequency fluctuations integrated on a small time step are given by the LHS of (8) and (11). The anelastic fluctuations depicted by the RHS of (8) and (11) are represented by RU and RP. These terms along with (14)–(17) are integrated on the long time step.

For the grid spacing of 750 m used in this study, a long time step of 6 s was used in conjunction with a short time step of 0.325 s.

e. Lateral boundary conditions

The placement of lateral boundaries about a modeled circulation is perhaps the most artificial aspect of a limited area model. More often than not, the lateral boundary is merely a guess of how the environment surrounding the domain of simulation interacts with the circulation within. The outlying region, such as that about a convective thunderstorm, might respond to lowering pressure at low levels produced by the storm by supplying low-level moisture to the storm, or if the storm is in competition with other cells some distance away, the large scale may cut off moisture to the cell. Mesoscale flow fields may induce horizontal convergence across the domain to enhance vertical motion or moisture supplies within the domain, or they may initiate internal gravity waves affecting stability locally within the domain. Hence the choice of a lateral boundary condition is critical to the simulation outcome and should be considered as a factor when interpreting the results of a simulation and comparing to observations.

The choice of boundary conditions then is a decision of how to assume the modeled circulation interacts with the surroundings. Since the circulation field outside the domain is often unknown to small-scale modelers, it is generally best to assume that an isolated thunderstorm is being modeled and the environment responds only to the modeled storm. It is also desirable to allow wave phenomena traveling within the domain to pass as freely as possible through the boundaries. The constraint of integral quantities, such as mass of air or water or energy

to constant magnitudes is often undesirable especially if the modeled disturbance is as vigorous as deep cumulonimbus convection. In fact, fluctuations in these integral quantities are the mechanisms by which the cumulus scale may modulate larger scale mesoscale or synoptic scale flows. Unfortunately, since the response of the larger scale systems to the domain scale integral variations is unknown, unchecked trends in these quantities may result and must be interpreted as such.

In order to allow internal gravity waves to pass out of the domain with as little reflection as possible and allow environmental quantities to fluctuate in a controlled manner at the boundaries, the Klemp-Wilhelmson (1978a, hereafter referred to as KW) set of lateral boundary conditions was used in this model. At outflow lateral boundaries, all advective terms were calculated upstream except the normal velocity defined on the boundary. At inflow lateral boundaries advective terms for all variables except the normal velocity were set to zero. The local change of the normal velocity at the boundary is specified by

$$\frac{\partial \bar{u}}{\partial t} = -(\bar{u} + c) \frac{\partial \bar{u}}{\partial x}, \qquad (36)$$

where c is the phase speed of the dominant internal wave directed out and normal to the boundary. KW found $c = NH/\pi$, where N is the Brunt-Väisälä frequency and H is a scale height, to be an appropriate value to minimize reflection of internal waves. In this study, a value of 30 m s^{-1} was used which is typical of the stability in the lowest 10 km of the troposphere. The $\partial u/\partial x$ term is calculated as a one-sided difference within the domain. If the value of u exceeds c and is of opposite sign, $\partial u/\partial t$ is set to zero. Turbulence fluxes of all quantities are specified to be zero at the lateral boundaries.

The boundary conditions described are slightly different from those of KW. Because KW dropped the advection and turbulence flux divergence in the pressure equation, no specification of a pressure derivative at the lateral boundaries was necessary. In this study, however, the advection and turbulence flux divergence were retained in (4) and therefore treated as the other variables discussed above.

These boundary conditions allow flow convergence or divergence to develop across the domain in response to the internal circulation. The resulting domain-wide mass variations, however, are not compensated by pressure-gradient-produced flows across the lateral boundary and hence trends in the net mass field may develop.

Recently, Clark (1979) reported on results of three-dimensional numerical experiments using the KW and Orlanski (1976) lateral boundary conditions. Clark concluded that the KW boundary con-

ditions produce computationally excited physical modes which result in very large horizontally averaged vertical velocities. Because this is a legitimate concern in this investigation, we further analyze the effects of the boundary conditions in Section 7.

f. Vertical boundary conditions

The lowest grid box is located such that its lower edge is on the surface. The $\bar{w}$ is defined at that point to be zero always. Second-order differencing is performed at the lowest grid box centered at $z = \Delta z/2$ and the highest grid box centered at $z = H - \Delta z/2$, where H is the top of the domain. If the sum of $\bar{w}$ and the terminal velocity of rain (v_T) is negative at the lowest grid point, rain advection is calculated using an upstream difference. This is done to help suppress the $2\Delta x$ vertical wave mode which tends to form in rainwater which constantly falls toward a fixed zero value. These conditions eliminate the need to define any variable immediately above or below the model domain.

The turbulent fluxes of $\overline{u''w''}$, $\overline{v''w''}$, $\overline{w''^2}$, $\overline{w''\theta''}$ and $\overline{q''w''}$ are specified at the lower boundary using the surface layer parameterization of momentum, moisture and heat described by Manton and Cotton (1977). It is assumed that the observed surface temperature and moisture remain constant and tend to restore departures produced by the storm circulation. As a consequence, surface cooling by cloud shadowing and wetting by precipitation is not considered in this study. The other turbulent fluxes of $\overline{w''q_c''}$, $\overline{w''q_r''}$ and $\overline{w''p''}$ are assumed zero at the surface and all vertical fluxes are assumed zero at the model top.

g. Model initialization procedure

The initial model conditions include a horizontally homogeneous basic state which is perturbed by moisture anomalies and the inclusion of divergence fields.

The basic state pressure, temperature and humidity were derived from a specified sounding (described in Section 3) by spline fitting the temperature and humidity profiles to the corresponding pressure profile. This was accomplished using a spline under tension routine programmed by Cicely Ridley of NCAR using mathematical methods described by Schweikert (1966). A tension parameter of 0.2 was used. Then, by assuming a hydrostatic variation in pressure,

$$P_0(z + \Delta z)$$

$$= P_0(z) \exp\left\{\frac{g\,\Delta z}{0.5R[T_{v0}(z) + T_{v0}(z + \Delta z)]}\right\}, \quad (37)$$

the pressure was integrated vertically from the

observed surface values to the given model-level heights. This is done by iterating between the spline-fit temperature and humidity values and the resulting pressure at each level until the pressure, temperature and humidity are within some tolerance range of satisfying (42). At the same time, the temperature and humidity must lie on the spline produced by the observed sounding. Basic state density and potential temperature are then derived from the temperature, humidity and pressure using (3) and (5). The basic state wind profiles are obtained at model levels by a simple linear interpolation of winds at observation heights. The composite wind profile used is described in Section 3.

In order to cause a cloud to form, the basic state is perturbed by the artificial insertion of a region of saturated air into the domain, the location and size of which is variable. The bubble contains a cylindrical region in which the air moisture is set to saturation. Below the saturated region, the water vapor mixing ratio is taken to change linearly from the saturated mixing ratio at the base of the saturated region to the observed surface moisture values. No perturbations are made to the potential temperature, or pressure. The resulting weak virtual temperature anomaly is sufficient to initiate buoyant vertical motion. Since the air is already at saturation, latent heating begins immediately and a cumuliform cloud is initiated. Because the observed environmental temperature is maintained throughout the perturbation, the level of free convection (LFC) is synonymous with the lowest condensation level (LCL) at the time of initialization. Although this initialization procedure is somewhat unrealistic, similar degrees of artificiality have been used by Miller and Pearce (1974), Klemp and Wilhelmson (1978a) and others by the initiation of vertical motion through pure temperature anomalies. Because of the moist bubble initialization, higher equivalent potential temperatures are created at the cloud base region than would be experienced by ascent of environmental air from lower levels. It was felt that such an initialization process was necessary in order to initiate convection in the absence of local vertical motion of sufficient strength to force air above the LFC. In each of the experiments described in this paper, the saturated cylinder was placed in the domain center and was taken to be three grid boxes deep, i.e., 2250 m, 6 km in diameter and beginning at the second grid box which is based at 750 m MSL. The diameter of the bubble corresponds to the diameter of one of the more intense radar echoes observed on 17 July 1973.

Because it is desirable to simulate the effects of larger scale vertical motion, a method of initialization was developed which produced a horizontally homogeneous field of vertical motion. Assuming an initial vertical profile of vertical velocity w_m, the

horizontal divergence (DIV) is calculated in finite-difference form from the anelastic form of the continuity equation given below:

$$\frac{\partial u}{\partial x} + \frac{\partial v}{\partial y} = \text{DIV} = -\frac{\partial w_m}{\partial z} - \frac{w_m}{\rho_0}\frac{\partial \rho_0}{\partial z}. \quad (38)$$

Assuming 1) no change of wind at the center of the grid, 2) the horizontal wind direction is constant, and 3) the vertical component of vorticity is zero, u and v are then adjusted across the grid at each level to a given mean vertical wind profile. These constraints are met by altering the magnitude of the total wind only in the direction of the flow, thus obtaining the desired convergence without introducing vorticity.

Since it is often desirable to produce a cloud having a horizontal scale comparable to observed clouds, the initial horizontally uniform vertical motion field given by (38) is altered by a dynamic initialization procedure. Because very little is known about the actual distribution of vertical motion below embryonic towering cumuli, a simple disturbance, symmetric about the center point of the domain, was initiated. It is, therefore, assumed that a percentage of the mean horizontally homogeneous vertical motion is focused to occur strongly within the moist perturbation radius described above and weakly beyond. A weighting formula given by the expressions

$$\text{WT}(d) = \alpha_1 \left\{ \left(\frac{D}{R_W}\right)^2 \exp\left[-\left(\frac{d}{R_w}\right)^2\right] \right\}^{-1}, \quad (39)$$

$$\bar{w} = \text{WT} \cdot w_m, \quad (40)$$

was used to focus the vertical velocity to within the radius R_w, where d is the distance from the center of the grid, D the distance of the diagonal from the center of the grid to the domain corner, and α_1 a number which is the inverse of the domain integral of the term in large braces, and $\bar{w}$ is the initial redistributed velocity. By applying this weighting function, the mean vertical velocity over the domain is not affected. A balance such as in (37) is maintained by adding vertical velocity variation given by (40) over a period of integration of 5 min in equal increments at each time step. During this time, no other tendencies on $\bar{w}$ are permitted. In addition, only pressure gradient tendencies are permitted on u and v while only the tendencies on the left-hand side of (4) are permitted on pressure. The potential temperature and water mixing ratios are not allowed to change during the adjustment period. Also, the u and v wind components are held constant to their observed values at the grid point closest to the domain center in order to maintain an observed wind profile in that region of the simulation. After this period in which the vertical velocity field is adjusted,

all quantities are constrained in the same manner for an additional 5 min of integration to allow further dynamic adjustment.

During this adjustment period, the lateral boundary condition on the normal velocity is modified to become

$$\frac{\partial u}{\partial t}\bigg)_N = -c\left(\frac{\partial \bar{u}}{\partial x} + \frac{\partial \bar{v}}{\partial y} + \frac{\partial w_m}{\partial z} + \frac{w_m}{\rho_0}\frac{\partial \rho_0}{\partial z}\right). \quad (41)$$

The purpose of this boundary condition is to prevent the formation of large values of total divergence near the lateral boundaries during the adjustment period and, hence, the generation of acoustic waves. After the total adjustment time of 10 min, the perturbation pressure is reset to zero everywhere. Subsequently, all quantities were allowed to progress as described by Eqs. (1), (4) and (7)–(10). The entire adjustment procedure is designed to initiate a perturbing initial circulation on the cloud scale which is as free as possible of gravity and acoustic wave-induced noise, yet preserving, to the extent possible, the integrity of the observed vertical profiles of temperature, moisture and wind. Since the adjustment is accomplished with only the terms on the LHS of (1) and (4), the process occurs very rapidly. Because the elimination of the gravity and acoustic imbalances is the primary concern in creating a stable but not necessarily steady initial state, it was felt that a strictly nonadvected balance was sufficient.

3. Description of the case study day and basic-state data

It is the intent of this study to use the CSU three-dimensional cumulus model to simulate the behavior of deep convection in an environment depicted by observations on 17 July 1973. The afternoon of 17 July 1973 over South Florida was synoptically undisturbed and, as is typical, conditionally unstable. Winds near the surface were light southeasterly becoming easterly at mid-levels and somewhat stronger northeasterly aloft. Convective patterns associated with the sea breeze appeared early in the day producing the usual east and west coast lines of convection. Radar echoes at 1800 (all times GMT) are given in Fig. 1 depicting these convective lines. Simulations of the mesoscale response to the environment over South Florida on this day were performed by Pielke (personal communication) and resulted in the generation of sea breeze associated vertical motion patterns. The data collected at the FACE central observing site and the National Weather Service in Miami together with the Pielke mesoscale simulation of sea breeze activity provided the data base from which the numerical cloud simulations were performed.

Clearly, the extent of observations that were taken do not permit simulation of any one storm as each

FIG. 1. Miami NOAA/WSR-57 10 cm radar depiction and surface winds over South Florida for 1800 GMT 17 July 1973. Actual printed digits in echo regions correspond to radar-estimated rainfall rates in mm h^{-1}.

storm is different, and each is affected by its immediate environment and preceding convective activity. It is possible, however, to construct wind, temperature and humidity profiles which are consistent with observations and which were likely to be observed preceding storm formation. Furthermore, fields of vertical motion simulated with a mesoscale model might be used to depict likely divergence fields set up by the sea breeze circulations. Hence, a realistic examination of the variable behavior of convection in the observed South Florida environment can be made and inferences on the sensitivity of convective to horizontally varying low-level divergence and low-level shear may be drawn.

As mentioned in the previous section, a reference state sounding is used to depict the undisturbed atmosphere prior to convection. On 17 July 1973, thermodynamic soundings were taken at 1200 (I) at Miami and at 1430 GMT (II) and 1830 (III) at the FACE central site location. These soundings are given in Fig. 2. Close examination of these observations reveals that the temperature profiles are quite similar above 1000 mb, although I and III indicate the existence of a slight surface inversion. In the case of I, this may be attributed to the remnant effects of the nighttime land breeze, while in the case of III, the inversion may be related to a weak gust front associated with nearby convection. This is supported by the corresponding humidity profile indicating a sharp increase in moisture above 975 mb and the wind profile scenario, discussed later. It is evident from the moisture profiles that a great

deal of daytime moistening has occurred, probably in conjunction with widespread convective storms.

The wind was observed by the 1200 Miami radiosonde and numerous daytime PIBAL's released by the FACE program at the Central Observing Site. These observations are given in Figs. 3 and 4. The Central Site observations indicate a general increase in northerly flow from 1407 to 1710, after which a dramatic increase in southerly flow occurred at 1953. Likewise, a shift of the u component to stronger easterly flow occurred at 1953. This information, combined with the coincident observed dew point inversion and temperature inversion indicate the passage of a convective gust front.

Because the thermodynamic profile must be horizontally homogeneous in the model initial field, it was decided to use temperature and moisture profiles typical of the pre-storm environment. Therefore, the temperature and moisture observations of 1430 were used from the surface to 940 mb. The observed drying and cooling associated with the wind shift was modeled through evaporative down-
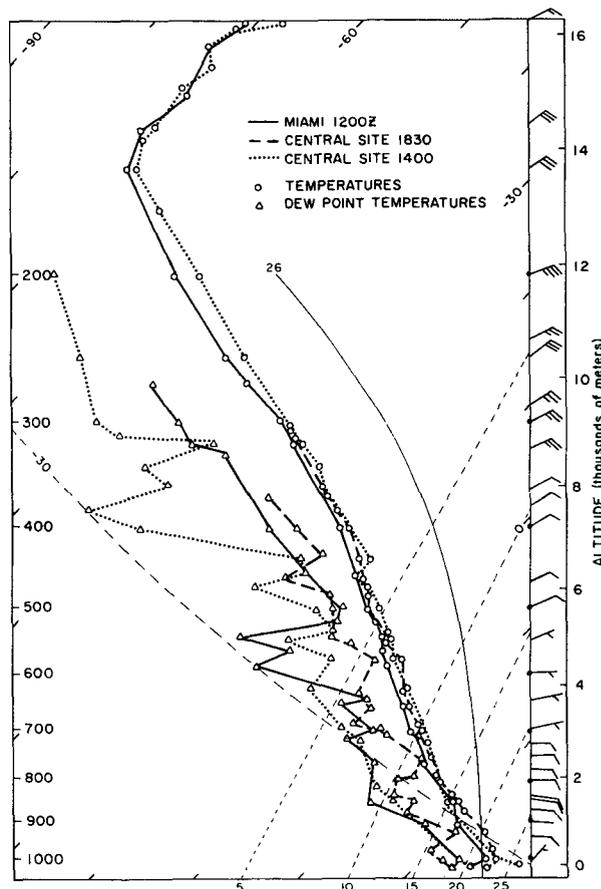

FIG. 2. Thermodynamic soundings taken at Miami 1200 GMT, and FACE Central Site 1430 and 1830 GMT, plotted on a skew-T log-P diagram. Miami winds are included, no Central Site winds were available. (Pressure in 10^{-1} KPa, temperatures in Kelvin.)
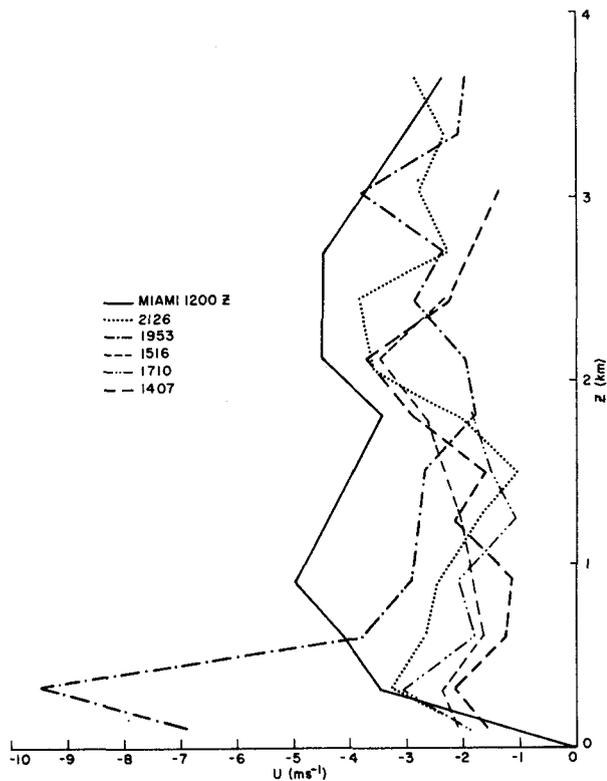
FIG. 3. U wind component observations taken by PIBAL at the FACE Central Site and Miami on 17 July 1973 for times indicated.

drafts that developed during the cloud simulation described below. Above 940 mb, the 1830 Central Site thermodynamic sounding was used to its observed height of 360 mb in order to include the effects of daytime cumulus moistening. Above 360 mb, the Miami sounding was used, since it matched closely with III at 360 mb where III terminated. The 1953 wind profile which includes the observed strong low-level wind shear was felt appropriate to a convective environment in which sustained deep convection is likely to occur. Above the 1953 PIBAL observation ceiling of 4 km, the 1200 Miami winds were used as the only available data source. The resulting composite thermodynamic sounding is illustrated in Fig. 5 and the composite wind profiles are given by Figs. 6 and 7. Note that an easterly wind of 4 m s^{-1} has been removed from the profile in order to keep the cloud centered as much as possible within the domain. The total wind is still employed in the surface friction formulation, however.

4. Description of numerical experiments

Cumulonimbus clouds over South Florida result from the interaction of all scales of atmospheric motion. Although the synoptically generated base state atmosphere sets the stage for convection,

mesoscale generated motions such as sea breeze circulations and squall lines or cumulus-scale motions such as gust fronts determine the precise nature of the convection present. Therefore any attempt to simulate a particular cumulonimbus circulation without a three-dimensional definition of prior mesoscale and cloud-scale circulations would be futile. The emphasis of the experiments of this paper, then, will be on studying the sensitivity of the cumulus structure, intensity, longevity and efficiency to variations in the environment of the storm. In particular, these experiments will address the sensitivity of cumulus activity to ambient mesoscale and cloud-scale environmental vertical motion. Also, additional experiments are performed to demonstrate the cloud sensitivity to some variations in cloud microphysics. In this manner, insight can be gained into the relative roles of these phenomena in the lifecycle of a cumulonimbus cloud in the South Florida environment.

The following series of numerical experiments were therefore performed:

(i) Experiment A: A cloud is initiated with the moisture perturbation described in (29) which is
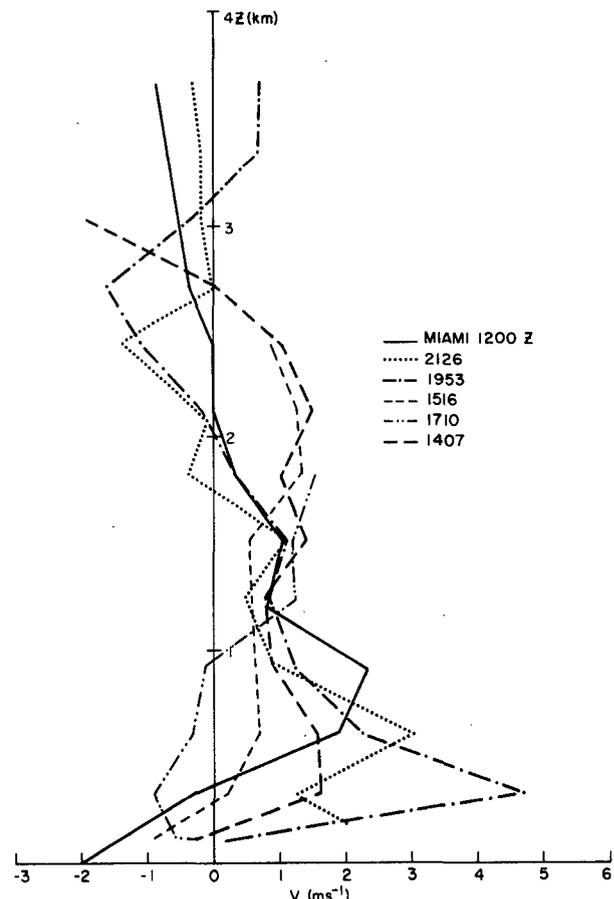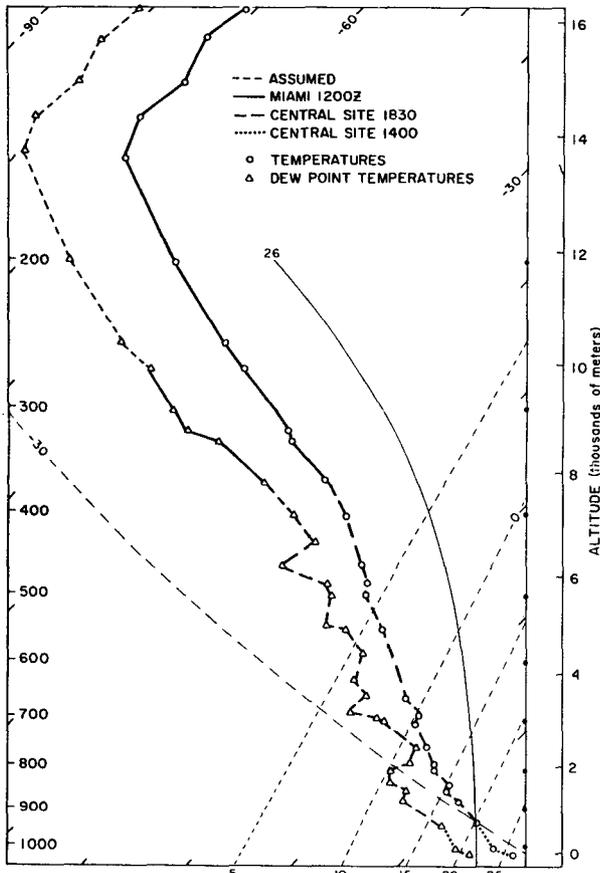

FIG. 4. As in Fig. 3 except for v component.

FIG. 5. Composite sounding used to initialize model based on three observed soundings given by Fig. 2 and some bogus dew-points above observed levels. Data sources for each section of the sounding are depicted by line type (Labels as in Fig. 2.)

2250 m deep, 6 km in diameter and beginning at the 750 m MSL level. There is zero mean convergence.

(ii) Experiment B: The mean moisture perturbation is as in experiment A. A mean vertical motion (w) field is imposed on the model based on preliminary numerical simulations of the Florida sea breeze on 17 July 1973 performed by Pielke (personal communication). Table 1 lists the profile of mean vertical motion obtained from his mesoscale model at a grid point in the vicinity of observed vigorous convection. The magnitude of the low-level convergence corresponding to the w profile is 1.87×10^{-4} s^{-1}. Using the focusing algorithm defined in Section 2g, 50% of the mean vertical motion given in Table 1 is then focused on the scale of the moisture anomaly defined in experiment A. This gives a peak initial $\bar{w}$ of 1.1 m s^{-1}.

(iii) Experiment C: This experiment is the same as experiment B, except 100% of the mean w is distributed on the cloud scale giving a peak $\bar{w}$ of 2.2 m s^{-1}.

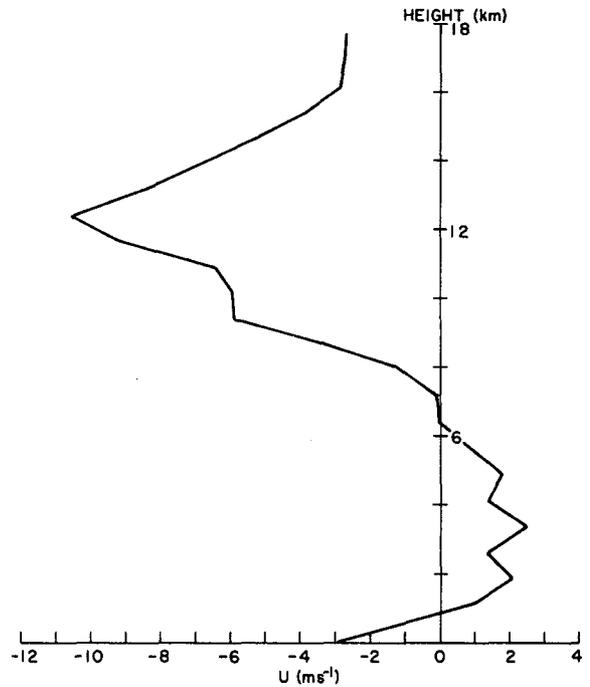(iv) Experiment D: As in experiment B except the mean convergence is doubled.

FIG. 6. Composite u profile used to initialize the model, with 4 m s^{-1} mean removed. Lowest 4 km from 1710 Central Site PIBAL and upper portion from Miami 1200 GMT sounding.

(v) Experiment E: As in experiment B, except the mean convergence is 3.5 times that used in B.

(vi) Experiment F: Miller (1978) found it necessary to nearly double the terminal velocity of rain in order
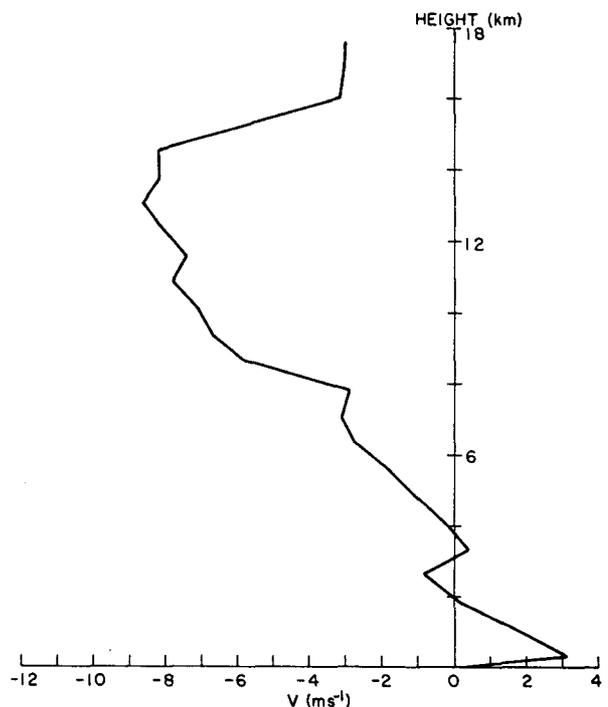

FIG. 7. As in Fig. 6 except for v component and no mean removed.

TABLE 1.

Height (m)	w_m (m s^{-1})	DIV (s^{-1})
0	0	
750	0.14	-18.7×10^{-5}
1500	0.11	$+4.0 \times 10^{-5}$
2250	0.05	$+8.0 \times 10^{-5}$
3000	0.02	$+4.0 \times 10^{-5}$
3750	0.0	$+2.7 \times 10^{-5}$
4500	0.0	0.0
5250	0.0	0.0

to initiate a steady, simulated storm circulation over Hampstead, England. He argued that the higher fallspeeds associated with hail would allow precipitation to escape from the updraft sufficiently rapidly to initiate a sustained storm circulation. Since hail is rarely observed at heights below the melting level in Florida summertime cumuli, the sensitivity of the cloud circulation to the presence of precipitation falling at hail speeds was tested by replacing (28) with

$$V_T = K\overline{q_r}^{1/6}\rho^{2/3} \qquad (42)$$

at levels above the melting level. This equation was used by Stephens[3] in his parameterization of hail processes in a cumulus model. With K equal to -3.38×10^{-4} m^3 kg$^{-2/3}$ s^{-1}, this formula can lead to fallspeeds twice as large as those obtained by (28). Experiment F, therefore, is identical to B except for the changes in v_T.

(vii) Experiment G: The sensitivity of the cloud circulation to the evaporation of rain in the subcloud layer is examined by enhancing the rain evaporation rate given by (35) by a factor of 10.

It must be recognized that in addition to the more obvious effects of large-scale vertical motion or focused uplifting in experiments B, C, D and E, associated changes in low-level (below 3 km MSL) wind speed and direction occur. These departures of the horizontal wind from the observed sounding are allowed to take place at all grid points at a given level, except at the very center of the initial disturbance where the observed wind profile is preserved. Thus, changes in the low-level, vertical shear of the horizontal wind must accompany alterations in the mapping in vertical motion.

5. Results

The results of the set of seven numerical experiments are described below.

a. Experiment A

This experiment was the first of the series of numerical experiments described herein. Since this represents a control experiment, only a brief summary of the more salient features of the simulation will be given here, while other features will be introduced in the discussion of subsequent experiments.

Initiation of a cloud with a moist bubble resulted in the formation of a single vigorous, short-lived convective cell. The simulated cloud exhibited a life cycle similar to that of the conceptual model of an airmass thunderstorm described by Byers and Braham (1948). Vertical velocities as high as 28 m s^{-1} and temperature anomalies in excess of 4°C developed in the rising bubble of moist air. Below the levels of high vertical velocity and temperature excess, horizontal convergence of air occurred through a deep layer in compensation for the strong vertical gradient of vertical mass flux (i.e., $\partial\rho w/\partial z$). At levels below cloud base, the horizontal convergence supplied moisture to the rising bubble, but this was diluted by the entrainment of dry air at levels above the original cloud-base height (750 m). Fig. 8 illustrates the resultant erosion of cloud base by the dynamic entrainment of dry air at levels above 750 m. The asymmetric nature of dynamic entrainment is illustrated in the horizontal map in Fig. 9. As shown in Fig. 10, on the upshear side of the cloud, a positive pressure anomaly is created which initiates a divergence of flow around the upshear-tilted updraft. In the downshear side of the cloud, a relative low pressure region or wake forms resulting in intense "dynamic entrainment." We use the term dynamic entrainment similar to Murray (1970), referring to entrainment resulting from the explicitly resolved circulation in the model. As found by Cotton and Tripoli (1978), the magnitude of eddy flux
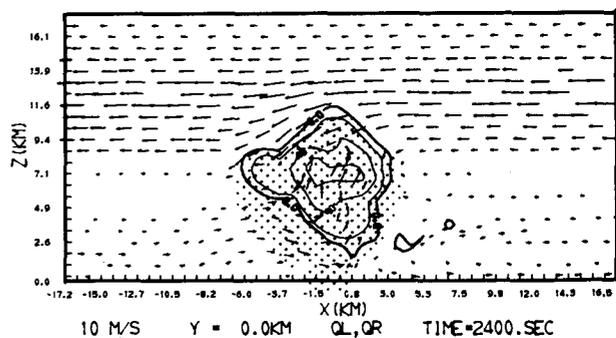

FIG. 8. East-west vertical cross section through center of initial perturbation at 2400 s for experiment A. Areas where rainwater exists are dotted and areas of cloud water are outlined by heavy solid line. Total liquid water ($\bar{q}_c + \bar{q}_r$) is contoured and labeled in g kg^{-1} $\times$ 10. Tracer arrows move with the relative wind; length is proportional to speed in the two-dimensional plane and is scaled as shown. Locations of model grid points are ticked along axis.
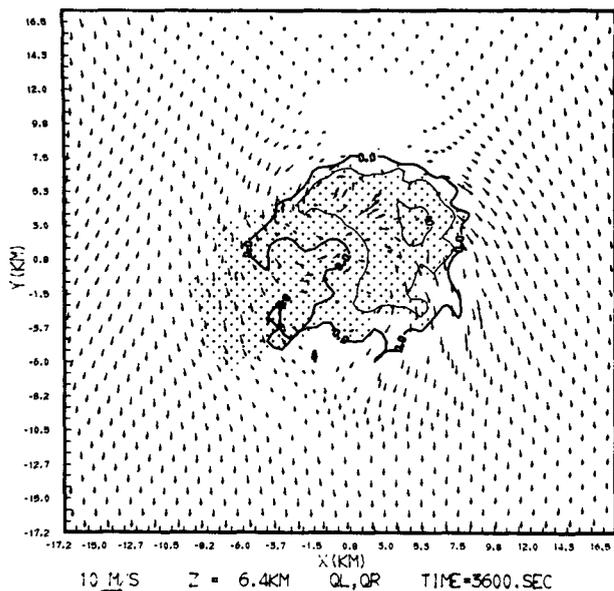
FIG. 9. As in Fig. 8 except horizontal cross section at 6.375 km MSL and at 3600 s time. (Y direction is north and X direction is east.)

divergence or turbulent entrainment, as modeled by the eddy diffusion terms (12), is generally three to four orders of magnitude smaller than the explicitly resolved flux divergences. In these numerical experiments, the dynamic entrainment rate is large enough to completely remove the liquid water content from a portion of the wake region. Such a circulation structure has been inferred by Heymsfield et al. (1978) and Ramond (1978).

An immediate consequence of the vigorous dynamic entrainment and associated erosion of the cloud base was that the low-level updraft was essentially terminated before the vigorous downdraft which was driven by evaporational cooling and rainwater loading entered the subcloud region. As a result, the coupled updraft/downdraft circulation that is essential to the formation of steady, long-lived convection (see Moncrieff and Miller, 1976) did not develop. Instead, the cool downdraft air diverged radially from the storm core at low levels with a slight tendency to favor the relative low pressure region to the north. As was found by Miller (1978), however, the highest surface convergence was produced along the relative inflow flank of the cell where weak outflow winds directly opposed the relative surface airflow. The forced vertical motion in that region was sufficient to force air above the LCL forming an arc cloud, but too weak to reach the level of free convection (LFC) some 2 km above. The production of rainfall thus decreased, the downdraft intensity weakened, and the cloud base rose leading to the rapid demise of the organized circulation on the cumulus scale.

The predicted time evolution of domain eddy kinetic energy and total surface rainfall for experiment A is shown in Figs. 11 and 12. The domain eddy kinetic energy relative to the moving reference frame is given by

$$KE = \frac{1}{2} \int_x \int_y \int_z \rho(\hat{u}^2 + \hat{v}^2 + \hat{w}^2)dxdydz,$$

where $\hat{u}$, $\hat{v}$, $\hat{w}$ represent the predicted air velocity components with the mean removed. The kinetic energy reaches a relative peak intensity associated with the maximum development of the initial moist bubble circulation. As the cloud base is eroded and the cloud circulation weakens, the kinetic energy gradually declines. Through 1 h of simulation, the total precipitation gradually accumulates to a magnitude of over 0.06×10^6 kg of water.

b. Experiment B

The combination of an imposed initial integral convergence of 1.87×10^{-4} s^{-1} and a focused vertical velocity with a peak amplitude of 1.1 m s^{-1} on the cloud-scale resulted in a much more sustained and vigorous cloud circulation. In contrast to experiment A, the predicted cloud base at 40 min illustrated in Fig. 13 has remained relatively firm across a considerable width of the cloud. Moreover, the initial updraft developed more quickly than in A. As in experiment A, the downdraft formed in the initial cloud circulation as a consequence of water loading and dynamic entrainment. This downdraft produced
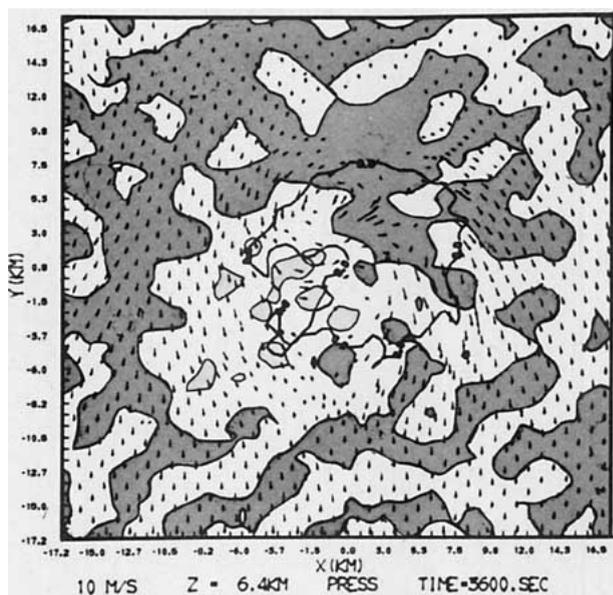

FIG. 10. Horizontal map of deviation pressure p' for experiment A at 6.4 km MSL and 3600 s time. Lightly shaded areas represent relative low pressure (<0.06 KPa) while darkly shaded areas represent relative high pressure (>0.08 KPa).
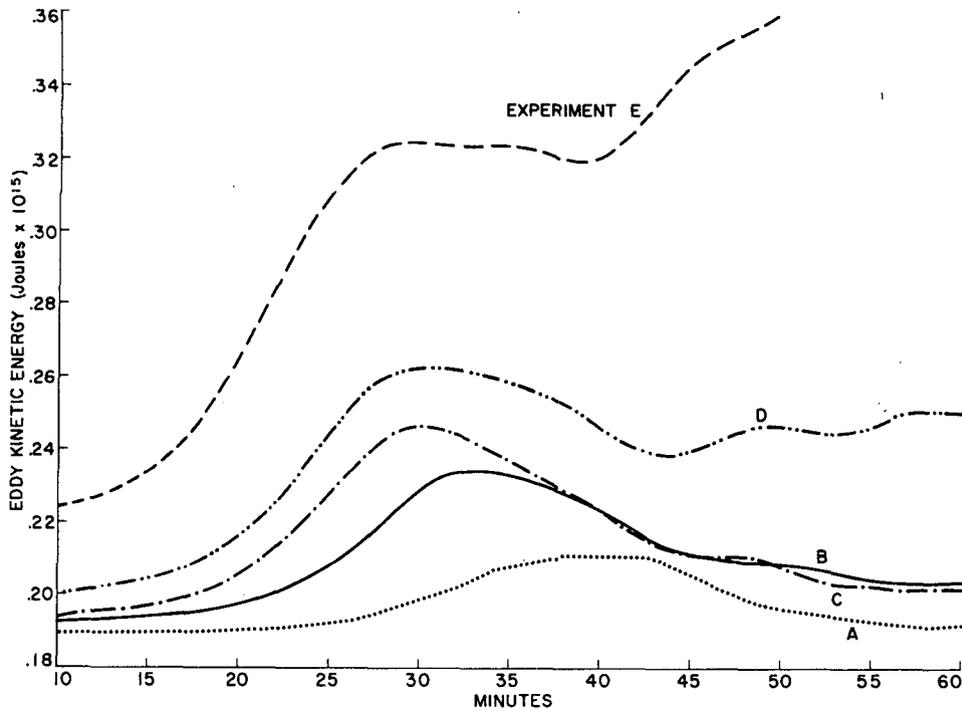
FIG. 11. Variation of domain eddy kinetic energy versus time for experiments A–E.

the strongest storm-induced convergence along the relative inflow (or southeastern) flank of the storm. The more intense downdraft in B, however, produced vertical motions along the southeastern flank large enough to lift air to the LCL as well as the LFC. Thus at 50 min, a new updraft can be seen in the eastern quadrant of the simulated storm (see Fig. 14a) as well as an updraft associated with the
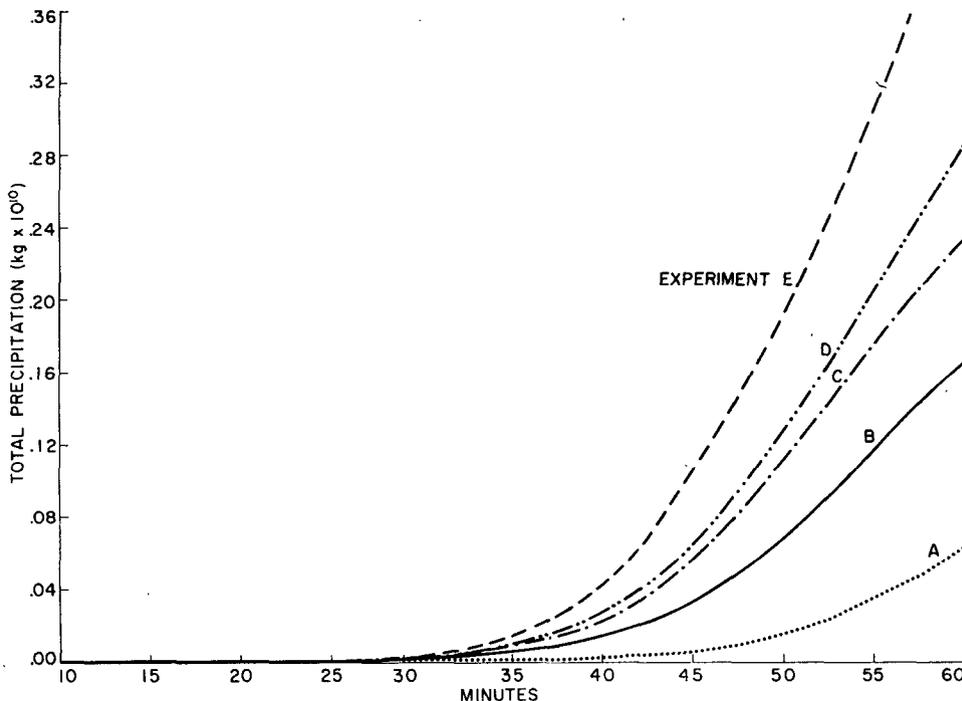

FIG. 12. Variation of total precipitation fallen within integration domain versus time for experiments A–E.
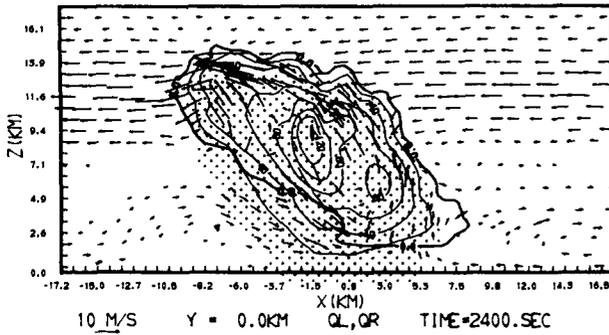
FIG. 13. As in Fig. 8 except for north-south cross section
for experiment B.

original circulation (see Fig. 14b) in the northern quadrant of the storm. By 50 min, the older updraft had become disconnected from the moist, low-level air and subsequently weakened, eventually turning into a downdraft throughout the region.

Strong divergence of the low-level flow about the region of heaviest precipitation can be seen in Fig. 14c. Driving this divergence is a relative high pressure region at the surface (see Fig. 15) which is generally colocated with the region of heaviest precipitation. Also noteworthy is the fact that a broad region of relative low pressure downstream of the region of high pressure was predicted. At 6.4 km MSL the primary maximum in total liquid water shown in Fig. 14d is associated with the parent updraft core. The secondary water maximum is associated with the new updraft located on the southeastern flank of the storm. Strong divergence is evident in the newer updraft indicating stronger upward mass transport from below. Also evident at this level is the relative inflow along the flank of the parent cell. This suggests that the parent updraft is beginning to decay.

By one hour, the dominant upward motion at the surface was positioned to the east and slightly north of the downdraft region. This updraft appears to be
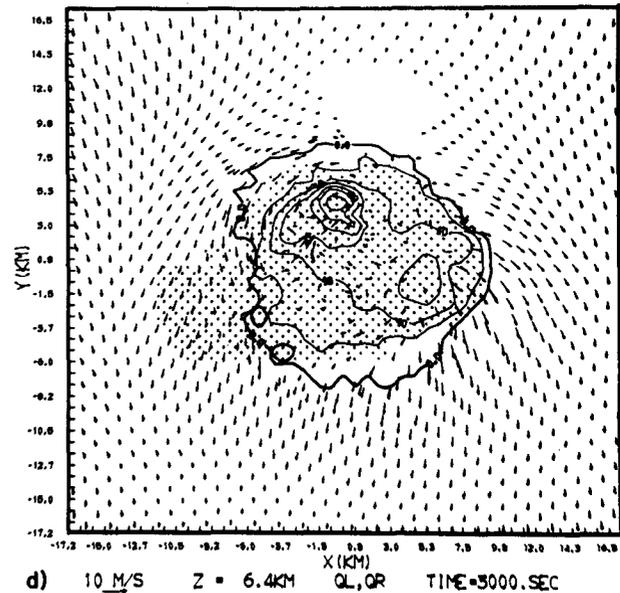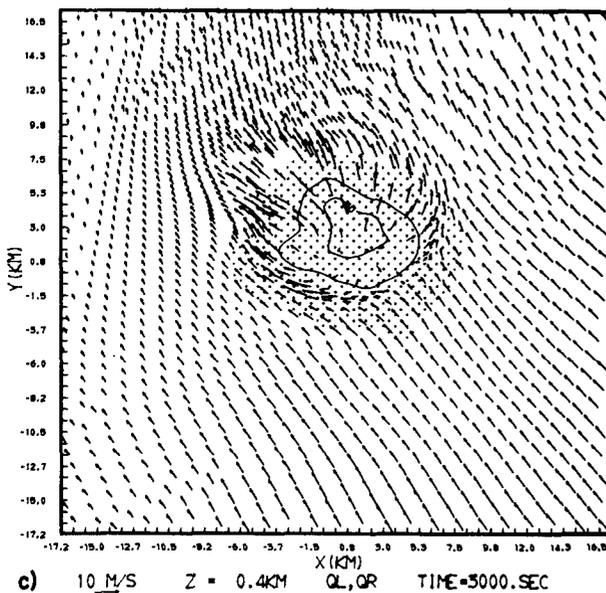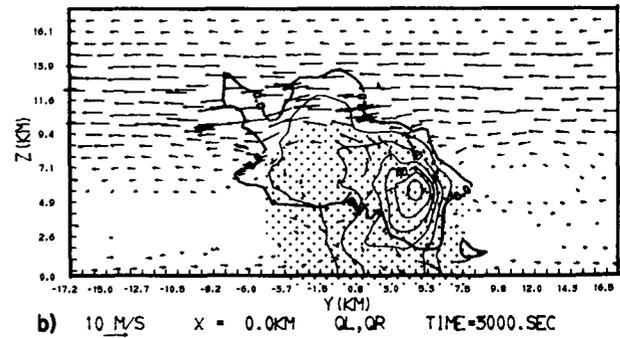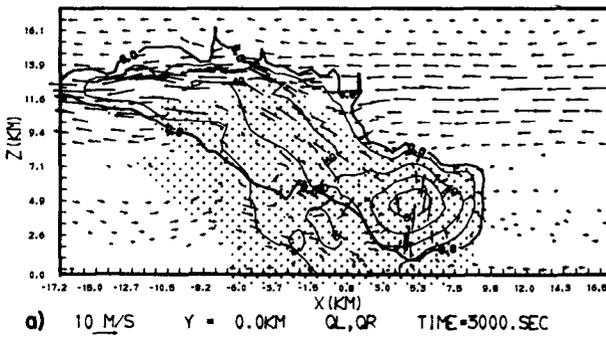

FIG. 14. Same as Fig. 8 except for experiment B at 3000 s and (a) east-west cross section, (b) north-south cross section, (c) horizontal cross section at 0.375 km MSL, and (d) horizontal cross section at 6.375 km MSL.
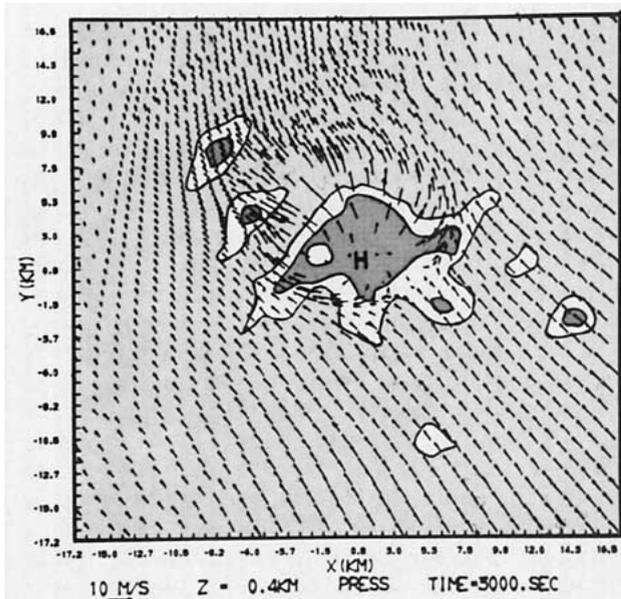
FIG. 15. Horizontal map of deviation pressure p' for experiment B at 0.4 km MSL and 3000 s time. Lightly shaded areas represent relative low pressure (<0.04 KPa) while darkly shaded areas represent relative high pressure (>0.06 KPa). A relative high pressure above 0.1 KPa is marked with an H.

the newer updraft referred to above, which had translated somewhat to the north. Peak vertical motions associated with the newer updraft, which formed on the relative inflow flank of the storm, were near 20 m s^{-1} compared to 28 m s^{-1} in the initial updraft. Likewise, peak temperature excesses were less: $3K$ in the secondary and $4K$ in the parent updraft. As a consequence, this multi-cellular storm circulation continued to weaken with time. This is dramatically illustrated in the kinetic energy curve shown in Fig. 11. As can be seen in Fig. 12, the initial convergence and focused vertical motion resulted in the prediction of nearly three times the precipitation predicted in experiment A at 1 h.

c. Experiment C

Experiment C differed from experiment B only in the way in which the large-scale vertical motion was initially distributed in the horizontal. In the case of C, 100% of the large-scale vertical motion was distributed on the cloud-scale, thus providing no initial upward motion near the lateral boundaries and 2.2 m s^{-1} in the center of the initial moist bubble. The locally enhanced upward motion led to a more vigorous initial circulation in C than in B. Many characteristics of the simulated cloud differed markedly from B, however. For example, at 30 min integration time, the cloud top in C reached above 12 km MSL compared to 9 km MSL for B. Experiment C also had greater horizontally averaged liquid water content than B reaching magnitudes of 8 g

kg^{-1} compared to 7 g kg^{-1} for B. Predicted horizontally averaged perturbation potential temperatures over cloudy areas in C were in excess of 4 K compared to 3 K for B. Rainfall amounts were ultimately greater than B also, although their total effect lagged in time behind those mentioned above. The results suggest that the initial updraft in C was somewhat less entrained with dry environmental air than that of B.

The inferred lower entrainment and greater vigor of the initial updraft led to significant structural differences between the circulation fields predicted in experiments C and B. Fig. 16 illustrates the structural features of the predicted circulation field in experiment C after 50 min of integration. Strikingly absent is the new resurgent updraft on the southeastern flank of the storm that was found in B. Instead, the initial updraft circulation continued to be rooted in the moist subcloud air in the northern quadrant of the storm (see Fig. 16b). As shown in Fig. 17, associated with the more vigorous initial cloud circulation and to the north of the area of low-level precipitation is a region of relatively low surface pressure. It appears that this region of low pressure diverted greater proportions of the downdraft air in C from the storm's southeastern flank to its northern flank. This further strengthened the original updraft circulation. The dominance of the single cell can be seen further in Fig. 16d in the total water field at 6.4 km MSL.

Interestingly enough, the ultimate level of kinetic energy in experiment C at 1 h was smaller than that experienced in B at the same time. Fig. 11 shows that C had a higher and earlier initial peak of kinetic energy, but by 40 min looked much the same as B. This suggests that although focused convergence may increase the intensity of a storm initially, or even alter its structure ultimately, after a time (here about 1 h) the domain eddy kinetic energy involved in the circulation, evolves to levels that are controlled by the magnitude of the integral convergence. Associated with the brief period of enhanced kinetic energy, however, is a significant enhancement of rainfall (see Fig. 12). The greater rainfall in C is probably a consequence of the lower entrainment in the updraft of the cloud.

d. Experiments D and E

To further examine the role of the integral convergence on simulated storm kinetic energy and rainfall, experiment B was repeated except that the mean convergence was doubled in experiment D and enhanced by a factor of 3.5 in experiment E. As in B, 50% of the mean vertical motion is distributed on the cloud scale thus giving a peak initial vertical velocity of 2.3 m s^{-1} in D and 4.1 m s^{-1} in E. The enhanced mean convergence in these experiments substantially altered the initial lower level wind field

a)   10 M/S   Y = 0.0KM   QL,QR   TIME=3000.SEC

b)   10 M/S   X = 0.0KM   QL,QR   TIME=3000.SEC

c)   10 M/S   Z = 0.4KM   QL,QR   TIME=3000.SEC

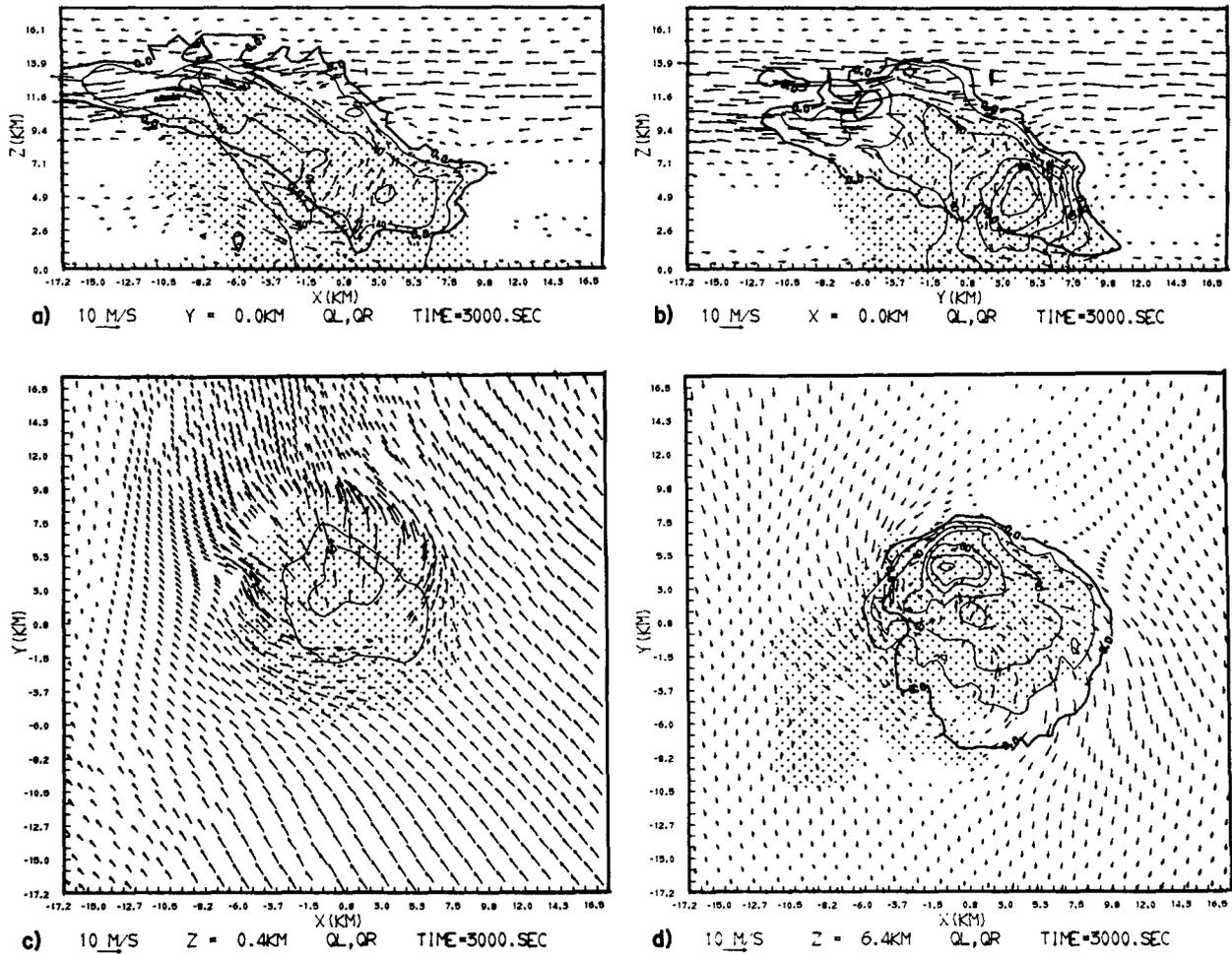d)   10 M/S   Z = 6.4KM   QL,QR   TIME=3000.SEC

FIG. 16. As in Fig. 8 except for experiment C at 3000 s and (a) east-west cross section, (b) north-south cross section, (c) horizontal cross section at 0.375 km MSL and (d) horizontal cross section at 6.375 km MSL.

except at the center of the domain where the wind profile was held fixed at observed magnitudes and directions during dynamic initialization. The convergence was large enough to reverse the initial lowest-level relative wind from one side of the domain to the other. This resulted in inflow at all the lowest level boundaries in both experiments.

The general organization of the simulated convective circulation in experiment D was similar in many respects to experiment C. The intensity of the storm, however, was greater than any of the preceding experiments. The original updraft in D remained strong during the formative stages of the downdraft and later reintensified from the lifting of the low-level outflow. As in C, the downdraft outflow was displaced more toward the north and northwest (as opposed to the southeast in A and B) due to the lower surface pressure in that region. A line of concentrated mean convergence formed with its long axis perpendicular to the direction of the mean low-level flow. This line of confluence was produced

by the nonlinear advection of the divergent part of the initial wind field. As can be seen in Fig. 18 the storm organization at 50 min is strongly influenced by the pre-existing line. Also of interest is the appearance of flow about an obstacle at low levels (Fig. 18a). The mean flow diverges about the heavy rain area and forms pockets of enhanced convergence along the "relative downstream" flanks of the precipitation zone. At 1.1 km MSL, Fig. 18b illustrates that the most intense convergence is associated with the original updraft cell.

The results of experiment E are generally similar to those of D, with the convective circulation of greater intensity than in D. As in D, the dominating influence of the preexisting convergence field is quite evident as can be seen in Fig. 19. The strong north-northeast to south-southwest orientation of the cloud line is quite evident after only 40 min of simulated time.

The time evolution of domain eddy kinetic energy and precipitation for experiments D and E are de-
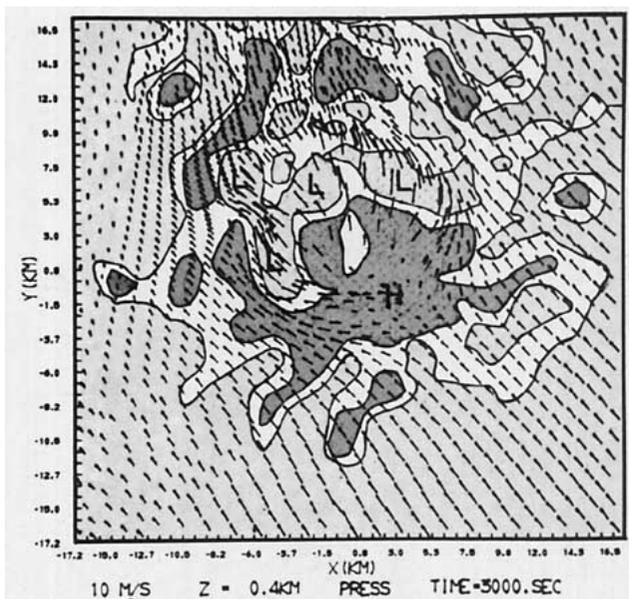
FIG. 17. Horizontal map of deviation pressure p' for experiment C at 0.4 km MSL and 3600 s time. Lightly shaded areas represent relative low pressure (<0.06 KPa) while darkly shaded areas represent relative high pressure (>0.08 KPa). High centers above 0.12 KPa are marked with an H, while low centers below 0.02 KPa are marked with L.

picted in Figs. 11 and 12. It is evident that greater amounts of convergence reduce the minimum in kinetic energy during the formative stages of the downdraft. In the case of E, the minimum of kinetic energy is only an inflection point, with the kinetic energy increasing in magnitude thereafter. This indicates that the initial moisture convergence is sufficient to supply moist static energy at the rate it was initially supplied by the moist perturbation. This maintains the initial convective circulation at a near constant energy level until the developing downdraft forces the circulation into an even greater rate of energy release. Eventually, the circulation encompasses too large a fraction of the model domain to be considered realistic. It is also obvious that total predicted rainfall amounts are highly dependent on the mean convergence.

e. Experiment F

Experiment F was the same as experiment B, except that above the 0°C isotherm the terminal velocity of precipitation was computed with (42), which simulated the fallspeeds of frozen rain and hail. In general, the resulting circulation was quite similar to experiment B. As expected, the most evident difference was that much smaller liquid water contents were experienced aloft in experiment F, and somewhat greater rainwater contents were predicted near the surface. In contrast to B, a notable increase in the size and strength of the

secondary circulation occurred along the southeastern flank of the storm. This was a consequence of the stronger and better organized uplifting that occurred along that flank.

The time evolution of total domain KE and total precipitation are given in Figs. 20 and 21. These plots closely resemble experiment B, except precipitation has increased slightly. The higher precipitation is probably a consequence of the more rapid transport of precipitation into the wet cloudy region below the 0°C isotherm before the initial updraft circulation terminated.
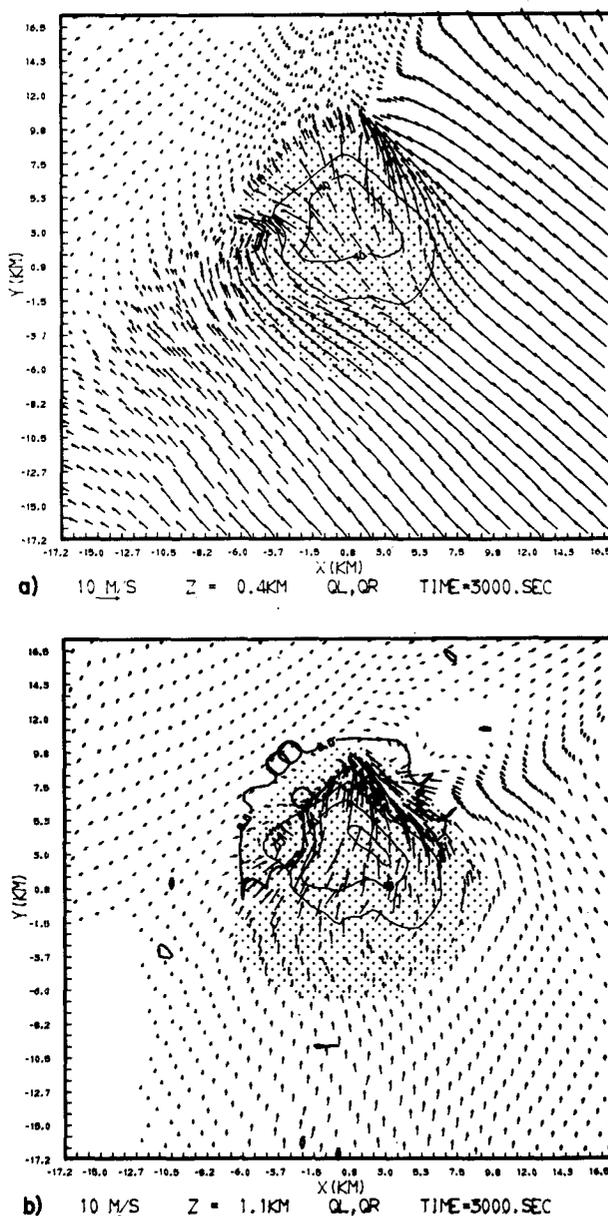

FIG. 18. As in Fig. 8 except for experiment D at 3000 s and (a) horizontal cross section at 0.375 km MSL and (b) horizontal cross section at 1.125 km MSL.
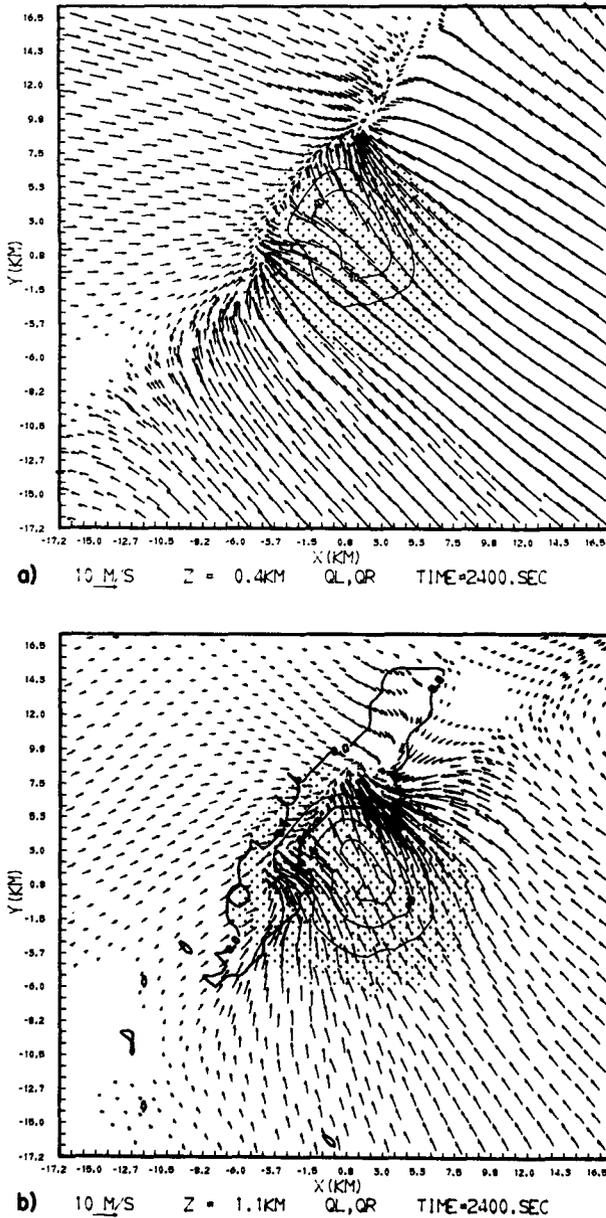
FIG. 19. As in Fig. 8 except for experiment E at 2400 s and (a) horizontal cross section at 0.375 km MSL and (b) horizontal cross section at 1.125 km MSL.

f. Experiment G

Because the evaporation of raindrops played an important role in the formation of a secondary updraft on the southeastern flank of the initial cell in experiment B, it was decided to determine the sensitivity of the model to alterations in evaporation rate. Therefore, the evaporation rate given by (35) was increased by a factor of 10.

The circulation produced in G was again very similar to that in B except that the downdraft possessed greater strength below cloud base where

enhanced evaporational cooling took place. This led to stronger downdraft outflow which produced stronger convergence and enhanced uplifting along the southeastern flank of the cell.

It is interesting, however, that the kinetic energy given in (20) was only slightly increased over B and the total precipitation decreased. The loss in precipitation was a consequence of greater evaporation of precipitation before reaching the ground. Analysis of cross sections of the cloud circulation (not shown) showed that the resurgent updraft and downdraft appear to have the most steady nature of any of the experiments. It seems evident, therefore, that experiment G produced the most steady circulation of all the experiments using the net convergence given in experiment B, but at the expense of total rainfall.

6. Discussion of results and conclusions

The results of these numerical experiments show that the magnitude of surface convergence over a finite area (defined by the model domain) had a pronounced influence on the simulated storm circulation, the total kinetic energy of the storm and the total rainfall of the storm system. It was found that as the magnitude of preexisting low-level convergence was increased, the predicted total domain kinetic energy increased proportionally. Although the storm structure was also modulated by variations in the local distribution of initial forcing or by variations in microphysical parameters, the close tie between kinetic energy and low-level convergence showed surprisingly little modulation. It appears, then, that the intensity of a cumulonimbus system is primarily related to the amount of moist static energy supplied to the storm by mesoscale surface convergence. This is consistent with the findings of Ulanski and Garstang (1978a,b) who observed surface convergence prior to thunderstorm formation in nearly all cases over South Florida. They pointed out that the size of the area of low-level convergence is one of the most important factors determining the amount of convective rainfall. This suggests a probable relationship between cumulus rainfall and integral convergence such as found in the experiments reported on in this study.

The close relation between cumulus intensity and the supply of moist static energy on the mesoscale has long been an underlying assumption in numerous cumulus parameterization techniques. The schemes formulated by Arakawa and Schubert (1974) and Kuo (1965) explicitly consider this relation while convective-adjustment-type parameterizations, such as Kurihara (1973) and Kreitzberg and Perkey (1971), implicitly rely on larger scale moisture transport to conditionally destabilize the atmosphere. The above parameterization techniques were developed with
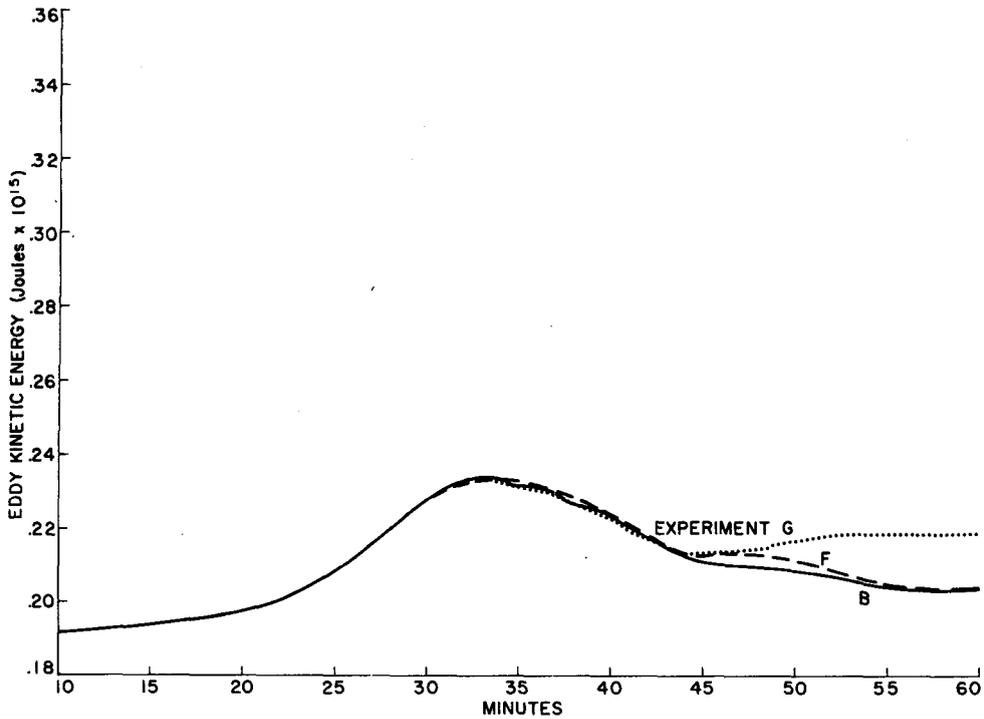
FIG. 20. Variation of total domain kinetic energy versus time for experiments B, F and G.

the ultimate purpose of modeling the larger scale response to subgrid-scale cumulus ensemble activity. In our own simulations, this response is handled in a very primitive manner by the KW boundary conditions. As a result, we can say little about meso-scale response to the time and space scales of a single modeled cloud.

Mesoscale convergence cannot be considered the only control on cumulonimbus duration and intensity. Certainly, modeling results of Moncrieff and
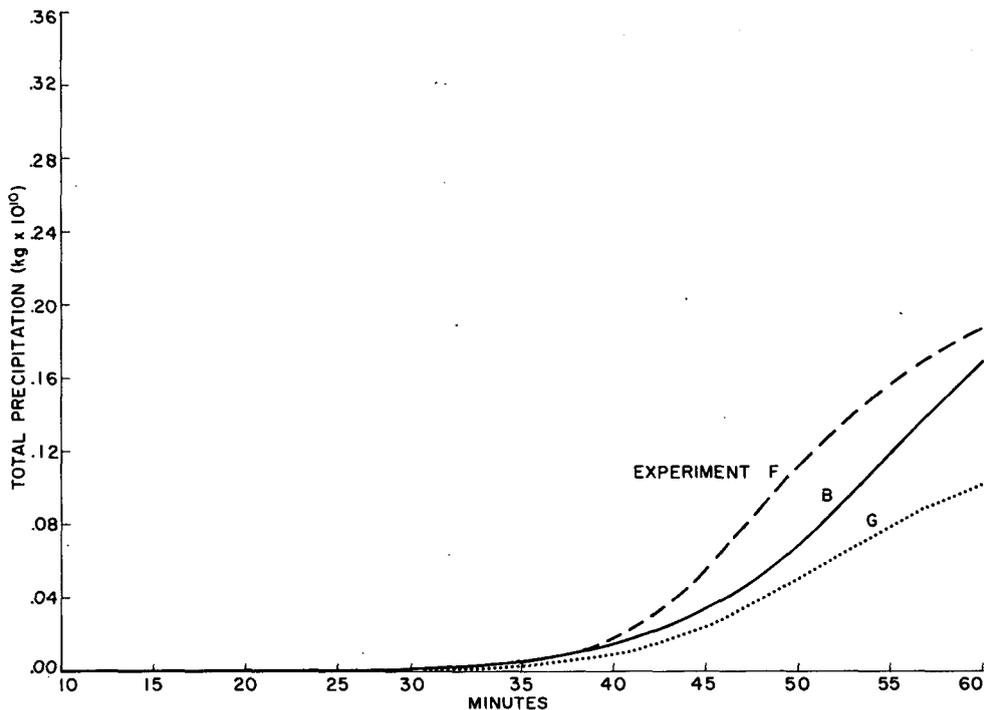

FIG. 21. Variation of total precipitation fallen within integration domain versus time for experiments B, F and G.
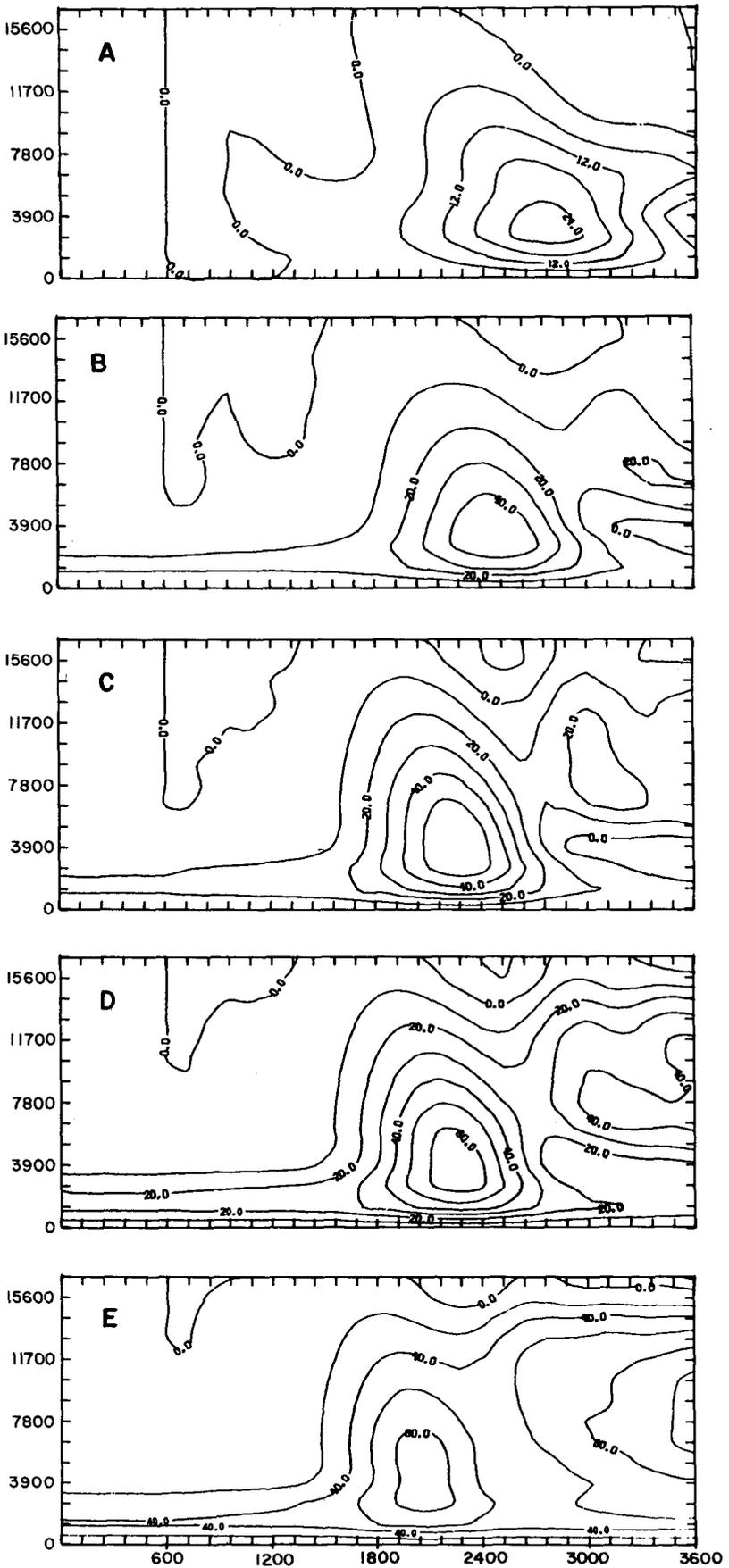
FIG. 22. Domain-averaged vertical velocity as a function of height and time for experiments A–E. Contours are labeled in cm s⁻¹ (10⁻² m s⁻¹).

Miller (1976), Miller (1978), Schlesinger (1978), Klemp and Wilhelmson (1978a,b) and Wilhelmson and Klemp (1978) have shown that sustained intense convection may occur without the presence of pre-existing mesoscale low-level convergence. It appears that the vertical shear of the horizontal wind may be responsible for increasing the low-level inflow to the cloud system. The relative inflow in turn supplies the storm with low-level moist static energy at rates sufficient to support the storm circulation.

The level of kinetic energy that can be maintained by a thunderstorm, therefore, is related primarily to the ability of the environment either to supply low-level inflow relative to the storm or to maintain sufficiently moist inflow by larger scale surface convergence. In any given storm both mechanisms (shear and convergence) must operate although one will likely dominate. In the moderately sheared environment considered in this study, shear-related inflow was most evident in experiment B where relative low-level winds supplied moisture to the southeastern flank of the storm. Apparently, this supply of moist static energy was not sufficient to sustain a steady storm system, however. Therefore, we conclude that the mesoscale convergence in these studies was the dominant mechanism responsible for the sustained intensity of the storm circulation.

The results of the numerical experiments with vertical motion initially focused on the cloud-scale suggest that within a given integral moisture convergence, the initial horizontal distribution of vertical motion can substantially alter the intensity and structure of the initial updraft circulation as well as the total amount of precipitation from the storm. A consequence of focusing greater amounts of mean convergence on the scale of the initial updraft is that the initial updraft is less severely inhibited by the destructive effects of low-level entrainment of relatively dry environmental air. Thus the initial updraft in experiment C exhibited higher temperatures and greater updraft speeds for a more sustained period than in experiment B. As a consequence, the predicted total precipitation in experiment C was ~50% greater than in experiment B.

An important feature of cumulonimbus circulations shown by these simulations was the varying relative importance of pressure gradient forces and momentum transport in the horizontal acceleration of momentum. The role of the buoyancy-driven updrafts and downdrafts in transporting horizontal momentum in cumulus circulations has been discussed extensively in the literature (e.g., Takeda, 1971; Miller, 1978; Thorpe and Miller, 1978, etc.). Moncrieff and Miller (1976), however, had shown an upgradient transport of momentum to occur within the deep cumulonimbus squall lines in the tropics. This horizontal acceleration of momentum in excess of the amount vertically transported can be attri-

buted to accelerations due to horizontal gradients of pressure on the cloud-scale. The simulations performed in this study show that horizontal pressure gradient forces are at least as important in accelerating winds as vertical transport of momentum.

It was apparent from each of the simulations performed that cloud-scale horizontal pressure gradients resulted in interesting interactions with the ambient horizontal flow field. Environmental horizontal flow was found to divert around the high pressure region associated with decelerating upward momentum of the updraft or decelerating downward momentum of the downdraft near the surface. In conjunction with this diversion of environmental air flow, the tendency for the formation of a "wake low" pressure region downstream of the forced high was evident.

At midlevels, the "wake low" pressure region was associated with increased entrainment of environmental air. The entrained air subsequently caused the evaporation of existing cloud water which, in turn, initiated a negatively buoyant downdraft in that region. Fig. 9 illustrates this process. This phenomenon has also been pointed out in previous studies by Heymsfield et al. (1978), Ramond (1978) and Cotton and Tripoli (1978).

At the surface, this "wake low" pressure region can cause the displacement of downdraft air in a direction opposite to that expected from simply vertical transport of horizontal momentum by convection. In experiments A and B, vertical transport of horizontal momentum was dominant within the low-level downdraft, which resulted in surface outflow convergence downshear, or in the southeast flank of the storm. As the initial updraft became more sustained in C, wake low pressure upshear was reinforced hydrostatically by heating aloft within the updraft and dynamically by low-level vertical acceleration of the updraft. As a result, a more significant portion of the outflow moved upshear demonstrating the greater importance of the pressure gradient force in accelerating the horizontal surface wind field. In experiments D and E, horizontal pressure gradient accelerations also dominated, again preventing any significant downshear surface convergence. This led to the sustenance of the initial forced cell with its updraft upshear rather than the development of a new updraft downshear as in A and B.

These results conclusively show that a stronger forced cumulus circulation will take on a more vigorous dynamical structure when pressure gradient forces tend to strengthen the existing structure. On the other hand, weakly forced circulations are dominated more by inertial accelerations which lead to discrete propagation of the updraft downshear, or along the relative inflow flank of the storm. It has been shown by numerous authors (i.e., Takeda,

1971; Klemp and Wilhelmson, 1978a,b; Wilhelmson and Klemp, 1978; Miller, 1978) that this secondary updraft downshear may also exist indefinitely provided that the downdraft-associated outflow convergence is of sufficient strength to maintain its low-level forcing.

Only small changes in the storm circulation, kinetic energy and rainfall occurred as a result of altering the terminal velocity of precipitation to that of hail at heights above the 0°C isotherm. Miller (1978) found that doubling the terminal velocity everywhere was sufficient to initiate a sustained cloud circulation. Due to the height of the melting level over South Florida and the large amounts of cloud liquid water at levels below the 0°C isotherm (the presence of cloud liquid water accelerates the melting process), we felt that altering v_T throughout the cloud was inappropriate for this study. Our results indicate that the higher freezing levels over South Florida diminish the dynamic effects of the ice phase discussed by Miller (1978). This does not diminish the potential effects due to the thermodynamic contribution of the ice phase which we are currently investigating numerically.

A tenfold increase in the evaporation rate of rain produced a marked increase in the intensity of the gust front and on subsequent storm organization. Since the enhanced evaporation of rain took place throughout the simulation duration, the increased storm vigor was at the expense of a 50% loss in precipitation.

It must be recognized that we have by no means exhausted the supply of factors which could have a significant influence on convective organization and intensity on a given day and at a given time over South Florida. For example, in our investigation of the influence of focused vertical motion within a mesoscale convergence field, we could also examine the importance of the area of focused vertical motion (it was held constant at 6 km diameter) or of the shape of the vertical motion field (i.e., lines of convergence or several areas of convergence). Moreover, the effects of variations in numerous microphysical factors could also be investigated.

7. Influence of boundary conditions

In a recent paper, Clark (1979) compared the results of numerical experiments using the KW lateral boundary conditions and boundary conditions developed by Orlanski (1976). He concluded that the KW contributed to unchecked trends in the predicted domain averaged vertical velocity $\langle w \rangle$ when applied to the Clark anelastic cloud model. Clark found that the KW boundary conditions resulted in a steady growth of $\langle w \rangle$, giving maximum values of $\langle w \rangle = 3$ m s^{-1} after 4800 s of computation. In comparison, he found that the Orlanski boundary conditions maintained a maximum $\langle w \rangle$ of ~0.75 m s^{-1} for the first 4000 s and then increased to 1.3 m s^{-1} after 5200 s of computation.

Because of the seriousness of these conclusions, $\langle w \rangle$ was computed as a function of height and time for each of experiments A–E and is illustrated in Fig. 22.

The time-height variation of $\langle w \rangle$ produced by experiment A shows a steady increase at mid levels until 2750 s where peak values of 0.24 m s^{-1} were reached. After this point, a general decay in $\langle w \rangle$ was found. Experiment B begins with a $\langle w \rangle$ of 0.2 m s^{-1} at low levels in response to initial mean convergence which grows to nearly 0.5 m s^{-1} at mid levels by 2400 s. Thereafter, a general decay of $\langle w \rangle$ takes place. Experiment C begins with the same $\langle w \rangle$ as B, but increases to peak magnitudes reaching 0.6 m s^{-1} before decaying to levels similar to B by 3600 s. As the initial prescribed $\langle w \rangle$ is increased further in experiments D and E, higher initial peaks of $\langle w \rangle$ occur in response to more vigorous cloud growth, followed by a general weakening of $\langle w \rangle$. There is evidence of a recovery of $\langle w \rangle$ to moderately higher values at the time those experiments were terminated. The initial peaks of $\langle w \rangle$ in each experiment can be attributed to vertical accelerations produced by both the moist bubble initialization, preexisting environmental conditional instability, and initially specified rates at which moist static energy is converged on the storm circulation. The extent to which a secondary recovery of $\langle w \rangle$ takes place is clearly related to the amount of initial mean convergence imposed. For example, in experiment E and to a lesser extent in experiment D, a secondary growth of $\langle w \rangle$ at the simulation end is taking place. This growth is due to intensification of upward motion within the domain due to the vertical transport of greater amounts of moist static energy converging across the boundaries. On the other hand, the circulations in experiments A–C cannot maintain initial levels of energy release with the given levels of mean convergence. As a consequence, $\langle w \rangle$ decreases.

Clark (1979) concluded that the KW boundary condition leads to the amplification of weak physical modes. In his own experiments, $\langle w \rangle$ reached values as high as 3 m s^{-1} in the presence of no preexisting convergence. Inspite of the fact that the convective circulation in the extreme case of our experiment E grew much too large with respect to the domain size, $\langle w \rangle$ reached values less than one-third those reported by Clark. It is, therefore, concluded that differences between $\langle w \rangle$ in the experiments reported on in this study are not due to trends produced by deficiencies in the KW lateral boundary conditions, but are closely related to the domain-scale convergence that was initially imposed.

8. Implications

The results of these numerical experiments have a number of implications to the concepts involved in the Florida Area Cumulus Experiment and to the interpretation of experimental results. First of all, the dominating influence of mesoscale convergence on predicted rainfall is clearly established. The extent to which cloud seeding (dynamic or static) can alter mesoscale convergence remains largely unknown and is certainly beyond the scope of this study. However, the ultimate potential of weather modification must lie with the ability to modulate mesoscale convective systems.

Combining these results with those of previous modeling studies (i.e., Takeda, 1971; Moncrieff and Miller, 1976; Miller, 1978; Schlesinger, 1978; Klemp and Wilhelmson, 1978a,b; Wilhelmson and Klemp, 1978; Thorpe and Miller, 1978), there is the suggestion that in a conditionally unstable atmosphere with a given low-level convergence, there is a greater opportunity for sustained, vigorous convection to form if the low-level wind shear is large. Conversely, one would expect that the weaker the low-level shear, the more dependent is the resultant convective intensity and precipitation on the magnitude of mesoscale convergence. It seems likely, therefore, that the opportunities are greater for obtaining significant enhancement of convective rainfall by "dynamic seeding" (see Simpson, *et al.*, 1965; Simpson and Wiggert, 1971) under conditions during which moderate intensity low-level wind shear is present. If the shear is weak, mesoscale convergence will dominate convective activity, whereas if the shear is intense, long-lived convective cells will form in moderate convergence regardless of whether or not seeding occurs. Our use of the term low-level shear refers to shear in the layer bounded by the main downdraft source levels (generally below 5 km MSL over South Florida) and the surface. A quantitative definition of what we mean by weak, moderate and intense shear must remain a subject for further investigation.

The results of experiments B and C imply that for a given mesoscale convergence and shear, there remains an opportunity to significantly alter the cloud circulation, enhance the updraft intensity and rainfall by enhancing the intensity of subcloud upward motion on the cloud-scale. Such focused updrafts on the cloud-scale could arise from a variety of natural phenomena including vigorous boundary-layer circulations, such as roll vortices, finestructure features of sea breeze or lake breeze fronts, local anomalies in topography or land use, and the intersection of outflow from previous convective cells. One might surmise, therefore, that in order for dynamic seeding to be effective on single and multiple clouds, subcloud vertical motion on the cloud-

scale must somehow be enhanced. These experiments suggest that the greatest opportunity for enhancing subcloud vertical motion is by enhancing the intensity of downdrafts in clouds that are already present. Perhaps what is perceived as a cloud merger (see Hess, 1974) is simply the intersection of outflows from neighboring cumuli. Simpson (1980) recently reached a similar conclusion based on observational evidence.

The numerical experiments in which the terminal velocity of precipitation and the evaporation rate of rain were altered have implications on the application of "static" seeding concepts to deep convective clouds. Suppose, for example, that the main response of seeding deep, towering cumuli is the transformation of precipitation from supercooled rain falling at modest fall velocities to higher terminal velocity frozen rain or small hail. The expected response would then be a precipitation increase on the order of 10% with little change in storm dynamics. Fig. 21 suggests, however, that even this amount of precipitation enhancement may be only temporary and that after another 30 min, the total precipitation is likely to be closer to the value predicted in the control experiment. If static seeding substantially increased the subcloud rainfall which, in turn, produced an enhancement in net evaporation of rain, then experiment G suggests that significant enhancement of the resultant storm dynamics may occur. It is doubtful, however, that a tenfold increase in net subcloud evaporation rate could be produced by static seeding.

The results described herein also have implications to convective parameterization theories for large-scale tropospheric models. The greater importance of cloud-scale pressure gradient forces over vertical transport of horizontal momentum to the resultant acceleration of horizontal winds has an important impact on the parameterization of horizontal momentum changes by convection. Clearly, the view that deep convection acts primarily to remove the ambient vertical gradient of horizontal momentum is not likely to be true, in general.

Experiment C implies that a mesoscale model with horizontal resolution on the order of 35 km and with a convection rainfall parameterization which is solely a function of mesoscale convergence, is likely to experience errors in predicted rainfall of at least 50%. Subgrid-scale anomalies in vertical motion could easily alter the resultant rainfall by such an amount.

The results discussed herein also have implications to the prediction of locally intense convective rainfall. Miller (1978) concluded that a slow-moving gust front formed by cumulonimbus downdraft outflow in a particular wind profile was primarily responsible for the formation of locally heavy rainfall over Hampstead, England. He argued that local

orography had no significant influence. Miller suggested that the convergence associated with the urban heat island over London may have been sufficient to isolate convection over London. Our results suggest that such a convergence induced by such a heat island may have played a more active role, perhaps controlling the rain volume of at least the parent cumulonimbi. Moreover, the fact that the maximum in rainfall coincided with a local hill (height ~ 120 m) may not have been fortuitous. Instead, the local hill could have played the role of the focused convergence in our simulations, thus creating an initially more vigorous and heavier raining parent cell. These factors along with a slow-moving gust front relative to the ground, all could have combined to create a locally intense rainfall event.

9. Summary

A number of sensitivity experiments employing a fully elastic three-dimensional cumulus cloud numerical model were performed using observed FACE data observed over South Florida on 17 July 1973. From the results of the numerical experiments, the following conclusions have been reached:

1) The ultimate level of kinetic energy which a single cumulus cloud can maintain is modulated by the level of preexisting low-level mesoscale convergence of moist static energy in a weak, low-level, sheared environment. This is consistent with recent observational results of Ulanski and Garstang (1978a,b).

2) The horizontal distribution of convergence has a relatively large effect on entrainment into the updraft below 5 km MSL. More highly concentrated convergence supplies the accelerating updraft with a greater fraction of source air from low-level very moist regions. This leads to higher predicted cloud temperatures and liquid water contents. As a result, more rain is also produced from the initial updraft.

3) Low pressure associated with a preexisting updraft will increase acceleration of outflow toward the relative position of that updraft. If that low pressure has sufficient strength, a greater portion of cool outflow air will be diverted beneath the parent updraft, thereby strengthening the updraft. If the pressure gradient associated with the existing updraft is too weak, a new updraft will form along the undisturbed relative inflow flank of the storm where vertical transport of horizontal momentum will force maximum convergence in that region. This resurgent updraft may reach the LFC if sufficient convergence is produced at low levels, and a large enough supply of moisture is brought in by the relative inflow.

4) High pressure associated with the updraft flow aloft and the converging downdraft at the surface diverts winds relative to the cloud around the pressure barrier. This produces relative low pressure in the lee of high pressure. At the surface, this forces a tendency to bias outflow acceleration downwind. Aloft, this may be a primary mechanism for enhancing dynamic entrainment and subsequent downdraft production in the relative lee of an updraft core.

5) Variations in terminal velocity associated with the introduction of the ice phase in themselves will have only a minor effect on increasing total precipitation and near-negligible effects on storm levels of kinetic energy. The greatest influence of higher ice fall velocities appears to be in creating a greater organization of the secondary updraft.

6) Increased rain evaporation rates lead to a much stronger low-level downdraft and resulting stronger secondary forcing. Any increase in efficiency due to stronger forcing appears to be countered by devastating losses of precipitation by evaporation. Some increase in kinetic energy was evident, but the effect was small when compared to those associated with variations in low-level convergence.

These conclusions are appropriate for single cumulonimbus clouds in the South Florida environment. Caution should be used in extending these results to groups of cumulus clouds for which additional considerations must be made.

APPENDIX

List of Symbols

ENGLISH

A	dummy variable
ACCR	accretion of cloud water by rainwater
ADJ	minimum upward isobaric saturation adjustment of cloud water
ADV	advective operator
AUTO	autoconversion of cloud water to rainwater
c	phase speed of dominant internal gravity wave
C_p	specific heat of air at constant pressure
C_v	specific heat of air at constant volume

d	horizontal distance from center of grid to a point
D	molecular diffusivity of water vapor
E	rain evaporation rate
E_{CR}	mean collection efficiency
e_s	saturation vapor pressure over liquid water
f_c	collision frequency for cloud droplets
f_i	Coriolis parameter in i direction
F	ventilation coefficient for falling raindrop
F_R	flux of rain mixing ratio relative to air
g	acceleration of gravity
$G(T,P)$	thermodynamic function
h	Heaviside step function
H	scale height of internal gravity waves
k	molecular diffusivity of heat
K	constant for estimate of hail terminal velocity
KE	domain eddy kinetic energy
L_{vl}	latent heat of vaporization of liquid water
m_w	molecular weight of water
N	Brunt-Väisälä frequency
N_0	intercept parameter for Marshall-Palmer distribution
N_c	cloud droplet concentration
N_R	rain droplet concentration
P	pressure
P_0	environmental pressure
P_R	reference pressure (1000 mb)
q_c	cloud water mixing ratio
q_r	rainwater mixing ratio
q_s	saturation over liquid water mixing ratio
q_v	water vapor mixing ratio
q_{cm}	threshold cloud water mixing ratio
r	rainwater droplet radius
R	dry-air gas constant
R_c	cloud water droplet radius
Re	Reynolds number
R_m	characteristic radius for rainwater distribution
R_w	assumed perturbation radius
R_*	universal gas constant
r_{cm}	threshold cloud water droplet radius
RP	nonacoustic tendency of pressure
RU_i	nonacoustic tendency of velocity
S	q_v/q_s
STK	Stokes number
t	time
T	temperature
T_0	environmental temperature
T_v	virtual temperature
u	velocity tensor in x direction
u_i	velocity tensor in i direction
v	velocity component in y direction
v_T	terminal velocity of raindrops
v_c	mean terminal velocity of cloud droplets
v_T	mass weighted average terminal velocity of raindrop distribution

w	velocity component in z direction
w_m	initial mesoscale value of w
WT	weighting function for focused convergence
x	Cartesian coordinate pointing east
x_i	coordinate tensor
y	Cartesian coordinate pointing north
z	Cartesian coordinate pointing up
$x(r)$	mass of droplet of radius r
$\bar{x}$	mean droplet mass

GREEK

α	parameter in rain parameterization
α_0	inverse environmental density $[=1/\rho_0]$
α_1	normalization function for focused convergence initialization
γ	C_p/C_v
δ_m	saturation delta function
ϵ	ratio of molecular weight of water to air (0.622)
κ	R/C_p
θ	potential temperature
θ_0	environmental potential temperature
θ_v	virtual potential temperature
θ_{v0}	environmental virtual potential temperature
μ	dynamic viscosity
ρ	density
ρ_0	environmental density
ρ_w	density of water liquid
ϕ	raindrop spectral density

REFERENCES

Arakawa, A., and W. H. Schubert, 1974: Interaction of a cumulus ensemble with the large-scale environment. 1. *J. Atmos. Sci.*, **31**, 674–701.

Beard, K. V., and S. N. Grover, 1974: Numerical collision efficiencies for small raindrops colliding with micron size particles. *J. Atmos. Sci.*, **31**, 543–550.

Blanchard, D. C., and A. T. Spencer, 1970: Experiments on the generation of raindrop size distributions by breakup. *J. Atmos. Sci.*, **27**, 101–108.

Byers, H. R., 1965: *Elements of Cloud Physics.* University of Chicago Press, 191 pp.

——, and R. R. Braham, 1949: *The Thunderstorms.* Govt. Printing Office, Washington, DC, 287 pp.

Chang, S. N., and H. D. Orville, 1973: Large scale convergence in a numerical cloud model. *J. Atmos. Sci.*, **30**, 947–950.

Chen, C.-H., and H. D. Orville, 1980: Effects of mesoscale on cloud convection. *J. Appl. Meteor.*, **19**, 256–274.

Clark, T. L., 1977: A small-scale dynamic model using a terrain-following coordinate transformation. *J. Comput. Phys.*, **24**, 186–215.

——, 1979: Numerical simulations with a three-dimensional cloud model: lateral boundary condition experiments and multicellular severe storm simulations. *J. Atmos. Sci.*, **36**, 2191–2215.

Cotton, W. R., 1972: Numerical simulation of precipitation development in supercooled cumuli, 2. *Mon. Wea. Rev.*, **100**, 764–784.

——, and G. J. Tripoli, 1978: Cumulus convection in shear flow-three-dimensional numerical experiments. *J. Atmos. Sci.*, **35**, 1503–1521.

——, R. A. Pielke and P. T. Gannon, 1976: Numerical experiments on the influence of the mesoscale circulation on the cumulus scale. *J. Atmos. Sci.*, **33**, 252–261.

Gal-Chen, T., and R. C. J. Somerville, 1975a: On the use of a coordinate transformation for the solution of the Navier Stokes equations. *J. Comput. Phys.*, **17**, 209–228.

——, and ——, 1975b: Numerical solution of the Navier Stokes equation with topography. *J. Comput. Phys.*, **17**, 276–310.

Grammeltvedt, A., 1969: A survey of finite difference schemes for the primitive equation for a barotropic fluid. *Mon. Wea. Rev.*, **97**, 383–404.

Gunn, R., and G. D. Kinzer, 1949: The terminal velocity of fall for waterdrops in stagnant air. *J. Meteor.*, **6**, 243–248.

Hess, W. M., 1974: *Weather and Climate Modification.* Wiley, 842 pp.

Heymsfield, A. J., D. M. Johnson and J. E. Dye, 1978: Observations of moist adiabatic ascent in northeast Colorado cumulus congestus clouds. *J. Atmos. Sci.*, **35**, 1689–1703.

Hudson, N. W., 1963: Raindrop size distribution in high intensity storms. *Rhodesian J. Agric. Res.*, **1**, 6–11.

Kessler, E., 1969: *On the Distribution and Continuity of Water Substance in Atmospheric Circulations.* Meteor. Monogr., No. 32, Amer. Meteor. Soc., 84 pp.

Klemp, J. B., and R. B. Wilhelmson, 1978a: The simulation of three-dimensional convective storm dynamics. *J. Atmos. Sci.*, **35**, 1070–1096.

——, and ——, 1978b: Simulations of right- and left-moving storms produced through storm splitting. *J. Atmos. Sci.*, **35**, 1097–1110.

Kreitzberg, C. W., and D. J. Perkey, 1976: Release of potential instability: Part I: A sequential plume model within a hydrostatic primitive equation model. *J. Atmos. Sci.*, **33**, 456–475.

Kuo, H. L., 1965: On formation and intensification of tropical cyclones through latent heat release by cumulus convection. *J. Atmos. Sci.*, **22**, 40–63.

Kurihara, Y., 1973: A scheme of moist convective adjustment. *Mon. Wea. Rev.*, **101**, 547–553.

Langmuir, I., 1948: The production of rain by chain-reaction in cumulus clouds at temperatures above freezing. *J. Meteor.*, **5**, 75.

Manton, M. J., and W. R. Cotton, 1977: Parameterization of the atmospheric surface layer. *J. Atmos. Sci.*, **34**, 331–334.

Marshall, J. S., and W. McK. Palmer, 1948: The distribution of raindrops with size. *J. Meteor.*, **5**, 165.

Miller, M. J., 1978: The Hampstead storm: A numerical simulation of a quasi-stationary cumulonimbus system. *Quart. J. Roy. Meteor. Soc.*, **104**, 413–427.

——, and R. P. Pearce, 1974: A three-dimensional primitive equation model of cumulonimbus convection. *Quart. J. Roy. Meteor. Soc.*, **100**, 133–154.

Moncrieff, M. W., and M. J. Miller, 1976: The dynamics and simulation of tropical cumulonimbus and squall lines. *Quart. J. Roy. Meteor. Soc.*, **102**, 373–394.

Murray, F. W., 1970: Numerical models of a tropical cumulus cloud with bilateral and axial symmetry. *Mon. Wea. Rev.*, **98**, 14–28.

Orlanski, I., 1976: A simple boundary condition for unbounded hyperbolic flows. *J. Comput. Phys.*, **21**, 251–269.

Pielke, R. A., 1974: A three-dimensional numerical model of sea breezes over South Florida. *Mon. Wea. Rev.*, **102**, 115–139.

Ramond, D., 1978: Pressure perturbations in deep convection. *J. Atmos. Sci.*, **35**, 1704–1711.

Schlesinger, R. E., 1978: A three-dimensional numerical model of an isolated thunderstorm: Part I. Comparative experiments for variable ambient wind shear. *J. Atmos. Sci.*, **35**, 690–713.

Schweikert, Daniel G., 1966: An interpolation curve using a spline under tension. *J. Math. Phys.*, **45**, 312–317.

Simpson, J., 1980: Downdrafts as linkages in dynamic cumulus seeding effects. *J. Appl. Meteor.*, **19**, 477–487.

——, and V. Wiggert, 1971: 1968 Florida seeding experiment: Numerical model results. *Mon. Wea. Rev.*, **99**, 87–118.

——, R. H. Simpson, D. A. Andrews and M. A. Easton, 1965: Experimental cumulus dynamics. *Rev. Geophys.*, **3**, 387–431.

Srivastava, R. C., 1978: Parameterization of raindrop size distributions. *J. Atmos. Sci.*, **35**, 108–117.

Takeda, T., 1971: Numerical simulation of a precipitating convective cloud: the formation of a long lasting cloud. *J. Atmos. Sci.*, **28**, 350–376.

Thorpe, A. J., and M. J. Miller, 1978: Numerical simulations showing the role of the downdraft in cumulonimbus motion and splitting. *Quart. J. Roy. Meteor. Soc.*, **104**, 873–893.

Ulanski, S. L., and M. Garstang, 1978a: The role of surface divergence and vorticity in the lifecycle of convective rainfall, Part I: Observations and analysis. *J. Atmos. Sci.*, **35**, 1047–1062.

——, and ——, 1978b: The role of surface divergence and vorticity in the lifecycle of convective rainfall, Part II: Descriptive model. *J. Atmos. Sci.*, **35**, 1063–1069.

Weickmann, H. K., and H. J. Aufm Kampe, 1953: Physical properties of cumulus clouds. *J. Meteor.*, **10**, 204.

Wilhelmson, R. B., and J. B. Klemp, 1978: A numerical study of storm splitting that leads to long-lived storms. *J. Atmos. Sci.*, **35**, 1974–1986.